AGU PUBLICATIONS

JGR

Journal of Geophysical Research: Earth Surface

RESEARCH ARTICLE

10.1002/2016JF004046

Coarse-grained debris flow dynamics on erodible beds

Stefano Lanzoni[1], **Carlo Gregoretti**[2], **and Laura Maria Stancanelli**[3]

[1]Department of Civil, Environmental and Architectural Engineering, University of Padua, Padua, Italy, [2]Department of Land, Environment, Agriculture and Forestry, University of Padua, Padua, Italy, [3]Department of Civil Engineering and Architecture, University of Catania, Catania, Italy

Key Points:
- Granular-liquid flow velocity profiles observed in flume experiments collapse if normalized by runoff velocity
- Dynamic similarity with field debris flows are reproduced in the laboratory with moderated scale effects associated with the reduced geometrical scale
- Granular-liquid flows over erodible beds show a spatially varied rheology consequent to the presence of different stress-generating mechanisms

Supporting Information:
- Supporting Information S1
- Data Set S1

Correspondence to:
S. Lanzoni,
stefano.lanzoni@unipd.it

Citation:
Lanzoni, S., C. Gregoretti, and L. M. Stancanelli (2017), Coarse-grained debris flow dynamics on erodible beds, *J. Geophys. Res. Earth Surf.*, *122*, 592–614, doi:10.1002/2016JF004046.

Received 3 AUG 2016
Accepted 9 FEB 2017
Accepted article online 21 FEB 2017
Published online 14 MAR 2017
Corrected 8 APR 2019

This article was corrected on 8 APR 2019. See the end of the full text for details.

Abstract A systematic set of flume experiments is used to investigate the features of velocity profiles within the body of coarse-grained debris flows and the dependence of the transport sediment concentration on the relevant parameters (runoff discharge, bed slope, grain size, and form). The flows are generated in a 10 m long laboratory flume, initially filled with a layer consisting of loose debris. After saturation, a prescribed water discharge is suddenly supplied over the granular bed, and the runoff triggers a debris flow wave that reaches nearly steady conditions. Three types of material have been used in the tests: gravel with mean grain size of 3 and 5 mm, and 3 mm glass spheres. Measured parameters included: triggering water discharge, volumetric sediment discharge, sediment concentration, flow depth, and velocity profiles. The dynamic similarity with full-sized debris flows is discussed on the basis of the relevant dimensionless parameters. Concentration data highlight the dependence on the slope angle and the importance of the quasi-static friction angle. The effects of flow rheology on the shape of velocity profiles are analyzed with attention to the role of different stress-generating mechanisms. A remarkable collapse of the dimensionless profiles is obtained by scaling the debris flow velocity with the runoff velocity, and a power law characterization is proposed following a heuristic approach. The shape of the profiles suggests a smooth transition between the different rheological regimes (collisional and frictional) that establish in the upper and lower regions of the flow and is compatible with the presence of multiple length scales dictated by the type of contacts (instantaneous or long lasting) between grains.

1. Introduction

Debris flows are rapid, gravity-induced mass movements consisting of sediment-liquid mixtures that propagate along channels incised into mountain slopes or debris fans. These movements represent a serious natural hazard due to the high velocity, the large volumes of mobilized sediment, and the high-impact forces exerted against any obstacle they come across. Understanding their mechanical behavior is a prerequisite for the design of suitable structures and countermeasures able to mitigate damages that, otherwise, could have a strong socioeconomic impact [*Thiene et al.*, 2016]. Debris flow behavior depends on the physical properties of the entrained sediment (size and aggregation), the amount of water runoff necessary to trigger the sediment motion and disperse the grains throughout the flow depth, and the altimetric and planimetric configurations of the conveying channel. All these factors contribute to determine the stress distribution and the corresponding deformation rate inside the moving solid-liquid mixture, thus controlling the formation, propagation, and deposition phases. The mechanical behavior of a debris flow is deeply embedded in the shape of the velocity profile, whose knowledge is fundamental for estimating the flow resistance coefficients in debris flow routing models [*Takahashi*, 1978; *Rickenmann et al.*, 2006; *Armanini et al.*, 2009; *Tiranti and Deangeli*, 2015; *Gregoretti et al.*, 2016a] and the rate of sediment entrainment [*Medina et al.*, 2008; *Iverson*, 2012; *Iverson and Ouyang*, 2015].

In the present contribution we are interested in a particular class of debris flows, called stony, made by mixtures of relatively coarse sediments and muddy water such that the internal stresses generated by grain collision tend to dominate [*Takahashi*, 2007]. They are usually triggered by high intensity and short duration rainfalls in headwater basins. Runoff with impulsive hydrograph descending from cliffs [*Kean et al.*, 2012; *Gregoretti et al.*, 2016b] impacts and mobilizes sediment laying at the rock base and in the channels incised on scree slopes, forming a solid-liquid mixture that routes downstream [*Berti and Simoni*, 2005; *Gregoretti and Dalla Fontana*, 2008; *Cannon et al.*, 2008; *Coe et al.*, 2008; *McCoy et al.*, 2012; *Kean et al.*, 2013].

Even though grain collisions are the primary source of shear stresses within stony debris flows, the overall mixture rheology is in general controlled by different overlapping mechanisms that prevent the use of a single rheological model throughout the entire flow depth [*Armanini et al.*, 2009, 2014]. In the upper layers of the front and the body, the flow is mainly controlled by shear stresses originating from interparticle collisions and solid-liquid interactions (collisional regime). Conversely, frictional contacts between grains lubricated by interstitial fluid prevail close to the static sediment bed (frictional regime). A transition layer typically forms between these two flow regions [*Armanini et al.*, 2009]. In addition, pore fluid pressure in excess of hydrostatic distribution can play a nonnegligible role when a significant amount of fine sediment is present in the mixture, affecting the properties of the interstitial fluid slurry [*Kaitna et al.*, 2016].

Various approaches have been proposed to tackle the complex problem of modeling the rheology of debris flows. *Bagnold* [1954] was the first to provide a constitutive equation for sediment-water mixtures. He attributed the reduction of flow resistance to the grain dispersion caused by interparticle collisions. This formulation relies on experimental coefficients obtained under the assumptions of elastic grains with a uniform arrangement. Later on, *Takahashi* [1978] applied Bagnold's constitutive equations to sediment-water mixtures flowing in open channels, proposing a dilatant two-phase model. The resulting constitutive equation accounts for collisional stresses in the upper part of the flow and quasi-static Coulomb friction stresses caused by enduring grain contacts near the bed, where the dynamical effects of the interstitial fluid are considered negligibly small. The experimental coefficients obtained by *Bagnold* [1954] are found to describe satisfactorily the flow over a rigid bed but have to be artificially tuned to simulate the sediment-water motion over an erodible bed [*Takahashi*, 1978]. To deal with this latter drawback, *Egashira et al.* [1997] proposed a relation for the static pore fluid pressure due to interparticle contacts. The resulting constitutive relation accounts for different boundary conditions (describing either a rigid or an erodible bed), as well as for variations along the flow depth of the stress-generating mechanism consequent to changes in the sediment concentration. More recently, *Iverson and Denlinger* [2001] developed a model in which frictional stresses within the solid phase are described by a Coulomb friction, mediated by pore fluid pressure according to Terzaghi's effective-stress principle, while viscous stresses are assumed to control the flow of the intergranular fluid phase. The mixture is thus modeled as a Coulomb solid in the limit of vanishing pore pressure and as a viscous fluid when pore pressure is large enough for complete liquefaction. Pore fluid pressure evolution is modeled through a forced diffusion equation, which reduces to a standard soil consolidation equation for cases in which the mixture is quasi-static [*Savage and Iverson*, 2003; *Iverson and George*, 2014].

According to the *GDRMiDi* [2004] group, dry dense granular flows may be described in terms of local friction and dilatancy laws, whereby the shear stress is proportional to the pressure through an effective friction coefficient entirely determined by the local conditions. This latter quantity and the solid volume fraction are functions of a single dimensionless shear rate parameter, the inertial number I [*da Cruz et al.*, 2005], representing the ratio of a microscopic timescale, typical of grain rearrangements, to the macroscopic timescale linked to the mean deformation, as well as the ratio of inertial forces to confining forces. These concepts have been subsequently extended by *Cassar et al.* [2005] to the case of submarine avalanches of granular material, assuming that the constitutive law obtained in the dry case still holds if the microscopic inertial time is replaced by a viscous timescale. The inertia parameter can thus be used to derive the uniform flow velocity profiles for given slope and flowing layer thickness, leading to a remarkable collapse of experimental data. An extension of these concepts has been recently proposed by *Armanini et al.* [2014]. Two coexisting physical mechanisms, interparticle collisions and friction, are assumed to sum together with different intensity as either the flow surface or the loose static sediment bed are approached. The heuristic model thus derived relies on a single dimensionless parameter, presumably determined by the contact properties of the interstitial fluid and sediments grains. When the model is applied to free surface flows over a mobile bed, it leads to two closure relations for the hydrodynamic resistance and the solid transport rate, to be calibrated experimentally [*Armanini*, 2015].

Flume experiments [e.g., *Takahashi*, 1978; *Mainali and Rajaratnam*, 1994; *Aragon and Juan*, 1995; *Egashira et al.*, 1997; *Gregoretti*, 2000; *Armanini et al.*, 2005; *Larcher et al.*, 2007; *Armanini et al.*, 2009; *Iverson et al.*, 2010; *de Haas et al.*, 2015], as well as classical rheometric tests [e.g., *Hanes and Inman*, 1985; *Major and Pierson*, 1992; *Coussot et al.*, 1998; *Contreras and Davies*, 2000] have been widely used to investigate the behavior of solid-liquid mixtures. Here we focus on flume experiments that, with respect to rheometric tests, have the advantage of including also the effects of gravity on normal stresses. Although flume experiments may suffer from scale effects that prevent the attainment of dynamic similarity over a broad range of scales (see section 4),

they are useful to gain physical insight into extremely complex processes. They have also the advantage of ensuring controlled initial and boundary conditions and allow the monitoring of quantities difficult to measure in the field.

Takahashi [1978], in his pioneering work, was the first to use flume experiments to investigate the rheological properties of sediment-water mixtures. Mature (i.e., with the grains dispersed throughout the entire flow depth) coarse-grained debris flows were generated in a 7 m long flume by using fine gravel, allowing the measurements of velocity profiles and mean sediment volumetric concentrations. Since then, many other researchers (see, e.g., the review by *Berzi et al.* [2010]) applied this methodological approach to study the dynamics of sediment-water mixtures. Here we recall the experiments of *Lanzoni* [1993], *Mainali and Rajaratnam* [1994], *Aragon and Juan* [1995], *Iverson et al.* [2010], *Armanini et al.* [2005, 2009], *Hsu et al.* [2008], *Kaitna et al.* [2014], and *de Haas et al.* [2015].

The extensive data set provided by *Lanzoni* [1993] constitutes the basis of the present study. It consists of 63 runs carried out on bed slope angles in the range 8–19° by using fine (3 and 5 mm) crushed gravel and 3 mm glass spheres (section 2). The data allow a systematic and thorough analysis of the velocity profiles within the body of the debris flow and of the corresponding bulk sediment concentration for a relatively wide range of bed slopes. These experiments, concerning coarse-grained debris flows produced in a medium size laboratory flume, can be regarded as intermediate between those carried out by *Mainali and Rajaratnam* [1994], *Aragon and Juan* [1995], and *Iverson et al.* [2010].

The contributions by *Mainali and Rajaratnam* [1994] and *Aragon and Juan* [1995], in fact, concern nearly steady flows of sand-water mixtures. The observed sand volumetric concentration (ranging in the interval 0.03–0.58) and velocity profiles (approximately logarithmic) indicate that highly concentrated suspensions rather than debris flows were attained in the experiments. Typical debris flow conditions were instead reproduced in the large scale experiments (17) carried out by *Iverson et al.* [2010] in a 95 m long, 2 m wide flume, with a rough fixed bed and a slope angle of 31°. The debris flow routing was created by releasing a saturated volume of a heterogeneous sediment mixture (sand-gravel and sand-gravel-mud) at the flume inlet. Owing to size-segregation phenomena, the debris flow front was formed by the larger grains and was characterized by larger voids.

Armanini et al. [2005] set up an experimental apparatus able to reproduce the flow of granular-liquid mixtures under temporally and spatially uniform conditions. The experimental facility was composed by a 6 m long, 0.2 m wide, glass-walled flume and by an external conveyor belt which supplied continuously water and sediment by recirculating them to the flume inlet. For each investigated slope, equilibrium conditions were found to be associated with a unique combination of solid and liquid discharges. The detailed analysis of sediment trajectories, facilitated by the temporal and spatial steadiness of the flow, highlighted the existence, close to the loose sediment bed, of a transition layer with an intermittent behavior, switching alternately from friction-dominated to collisional-dominated regimes. Steady flow conditions were also attained in the tests carried out by *Hsu et al.* [2008] and *Kaitna et al.* [2014] in a 4 m diameter rotating drum, by using five different gravel mixtures saturated with slurries composed of water and mud. Velocity profiles, flow depth, basal normal stress, and basal pore fluid pressure were the quantities measured in these tests. The effects of sediment composition on debris flow mechanics were also addressed by *de Haas et al.* [2015] by rapidly releasing a well-mixed volume of debris and water along a 2 m long and 0.12 m wide flume, ending with a lower angle sloping plane. The small-scale flows thus generated were found to be quite similar to natural debris flows in terms of bulk flow behavior, deposit morphology, grain size sorting, channel width-depth ratio, and runout.

The aim of the present contribution is to better clarify the role of quasi-static and collisional stresses in determining the velocity profile that establishes within the body of a coarse-grained debris flow flowing over an erodible bed. In particular, we want to assess which type of rheology is responsible for the observed profiles, and how much the information collected from flume experiments can be taken to be representative of field events. The analysis takes advantage of the systematic data set provided by *Lanzoni* [1993] and briefly documented by *Lanzoni and Tubino* [1993]. These data are thoroughly reviewed and validated. Observed velocity profiles and bulk transport concentration are used to quantify the dimensionless parameters that control the phenomenon, and to discuss the possible scale effects. We show that scaling the coordinate normal to the bed with the overall flow depth and the longitudinal component of the mixture velocity with the runoff velocity can determine a remarkable collapse of all the observed velocity profiles. The shape of these profiles suggests a gradual transition between the different rheological regimes (collisional and frictional) that establish in the

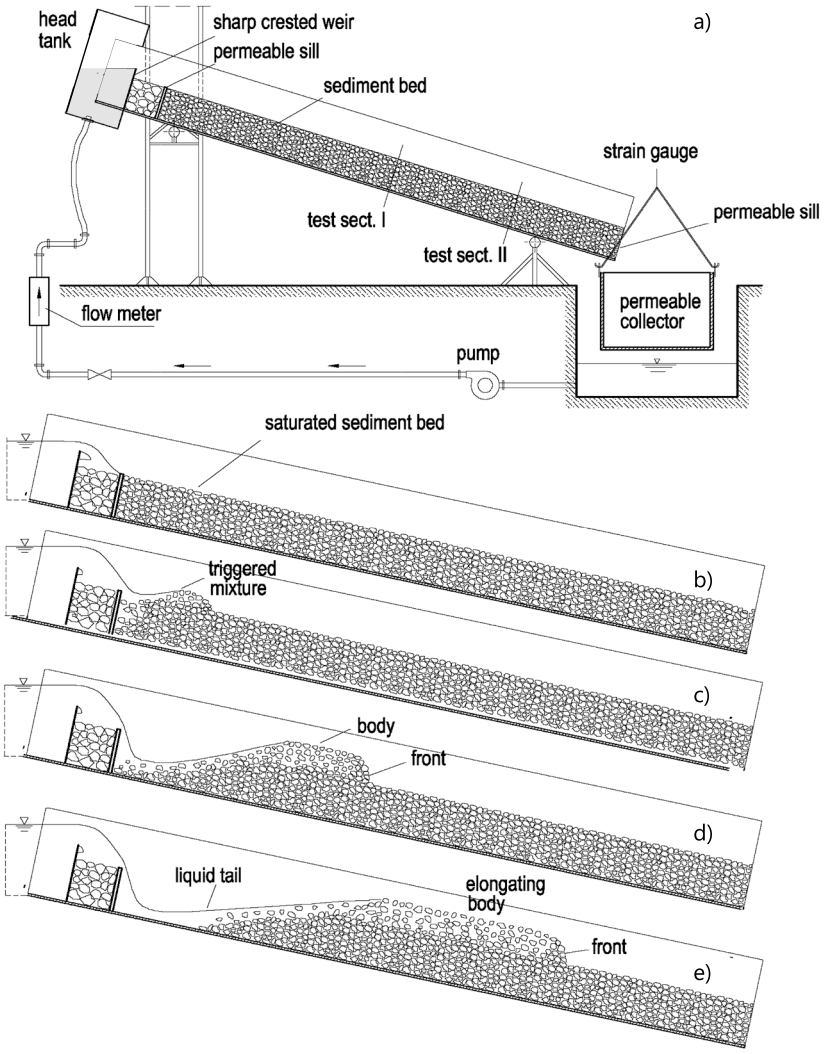

Figure 1. (a) Sketch of the experimental apparatus and (b–e) of the various phases characterizing the formation of a sediment-water wave flowing over a saturated loose granular bed.

upper and lower regions of the flow. The analysis of bulk transport concentration points out the importance of the quasi-static friction angle and the functional dependence of solid concentration from the slope angle. Finally, the influence of different stress-generating mechanisms is investigated by means of a coherence length approach, in analogy with the Prandtl mixing length model used to describe turbulent boundary layers.

2. Materials and Methods

2.1. Flume Tests

The tests analyzed in the present study were carried out in a 10.0 m long, 0.2 m wide and 0.3 m deep tilting flume, with polycarbonate walls (Figure 1a). A loose sediment layer of thickness about 0.1 m was placed inside the entire length of the flume before each test. The physical and mechanical characteristics of the adopted materials (3 and 5 mm crushed gravel, and 3 mm glass spheres) are reported in Table 1. In the case of crushed gravel, the bed slope angle θ considered in the tests ranged in the interval 10–19°, while an angle varying in the range 8–12° was considered in the runs with 3 mm glass spheres. A head tank equipped with a sharp crested weir supplied the water within the flume. An array of pebbles placed just downstream of the crested weir and retained by a metallic net was used to dissipate the energy of the inflowing water. The loose sediment bed was initially saturated by slowly releasing a water discharge Q_0 (Figure 1b). A permeable ground sill, located at the flume end, prevented the degradation of the sediment bed during saturation. The debris flow was subsequently triggered by sudden releasing on the head tank a preset water discharge Q_T (Figure 1c), that

Table 1. Physical and Mechanical Characteristics of the Material Adopted in the Flume Tests and Ranges of the Relevant Parameters [*Lanzoni*, 1993; *Lanzoni and Tubino*, 1993][a]

Material	d_s (mm)	ρ_s (kg/m^3)	C_{max}	φ_d (deg)	φ_s (deg)	φ_{qs} (deg)	θ (deg)	Q_T (l/s)	Q (l/s)	N_{tot}
Gravel (A)	5	2650	0.56	42	42.0	37.7	16–19	1.2–2.3	1.5–3.6	30
Gravel (B)	3	2650	0.58	43	42.7	36.1	16–19	1.2–2.3	1.5–3.1	17
Glass spheres (C)	3	2600	0.63	25	24.2	24.2	9–12	1.6–2.3	1.7–2.5	16

[a] d_s, mean diameter; ρ_s, density; C_{max}, closest packing sediment concentration; φ_d, dry repose angle; φ_s, submerged repose angle; φ_{qs}, quasi-static friction angle (see section 4.2); θ, bed slope angle; Q_T, triggering runoff discharge; Q, total water discharge; N_{tot}, total number of tests. The seepage discharge initially used to saturate the sediment bed is $Q_0 = Q - Q_T$. The values of φ_d and φ_s were determined through a tilting table, while C_{max} was estimated by measuring the volume occupied by a compacted dry sample and the amount of water (in volume) needed to fill the voids.

varied in the ranges 1.2-3.3 l/s for gravel, and 1.6-2.3 l/s for glass spheres. In particular, Q_T and θ were varied while holding the other parameters constant. The water overtopping the sharp crested weir plunged over the dissipating pebbles and flowed downstream, generating a runoff wave that propagated over the saturated loose bed, scouring it at a high rate and dispersing the entrained grains throughout the flow depth (Figure 1c). A progressive erosion and entrainment of grains occurred in the first part of the flume (~4 m), until enough material was provided for the formation of a debris flow front (Figure 1d). This front then propagated downstream with almost negligible erosion of the saturated sediment bed. Contemporaneously, the debris flow body elongated by the progressive entrainment of the material eroded at the tail (Figure 1e). Note that after the debris flow has fully formed (Figure 1d), part of the triggering discharge contributed to form a liquid tail behind the debris flow wave, as documented experimentally also by *Tognacca et al.* [2000] and assumed by *Takahashi* [1978] to model the initiation and development of debris flows due to bed erosion along a uniform sloping gully (see supporting information S1).

Two video cameras, working at 50 frames per second and oriented perpendicularly to the flume wall, were used to record the flow at two test sections, located 4.6 (section 1) and 2.2 m (section 2) upstream of the flume outlet (Figure 1a). During the passage of the debris flow body, no significant changes of the overall flow features were detected between these monitoring sections for a time interval ranging ~2–5 s. Indeed, the comparison of mean flow depth and velocity observed in the two monitoring sections suggests that a quasi-uniform condition was reached by the debris flow body, with minor differences at the two locations. Tests carried out under similar hydraulic conditions exhibited remarkably similar mean values of depth and velocity, indicating a high degree of repeatability of the tests.

2.2. Data Analysis

The runoff velocity U_0 associated with the triggering discharge Q_T has been estimated through a relation accounting for the strong interactions between the surface water flow and the roughness elements in the presence of low-submergence conditions. Following *Nikora et al.* [2001], we write

$$U_0 = \left[\frac{C_{ond}}{d_s} \sqrt{g \sin\theta} \left(\frac{Q_T}{B} \right)^{3/2} \right]^{2/5} \quad (1)$$

where B is the channel width, d_s is the mean grain size, g denotes the gravitational constant, and C_{ond} is a suitable conductance coefficient, set equal to 3.0 on the basis of the experiments carried out by *Gregoretti* [2008].

Longitudinal and normal components of the sediment velocity, u_p and v_p, were determined by analyzing particle trajectories from video records in an area of size 0.1 × 0.15 m when the overall flow depth was observed to attain a nearly constant value. The measuring area was divided in longitudinal layers of thickness $2d_s$ and the particle positions were tracked frame by frame (Figures 2a and 2b). The velocity components of particles belonging to the same layer were then averaged, obtaining the layer-averaged (i.e., binned) values $u(y) = \langle u_p \rangle(y)$ and $v(y) = \langle v_p \rangle(y)$, with y as the coordinate normal to the channel bed, pointing upward and originating at the surface of the initial sediment bed. The accuracy in evaluating these velocities is about 2×10^{-3} m/s. The binned component $\langle u_p \rangle$ is invariably positive, owing to the unidirectional character of the average flow, and the fluctuations $u_p' = u_p - \langle u_p \rangle$ are generally much smaller than $\langle u_p \rangle$. Conversely, the binned

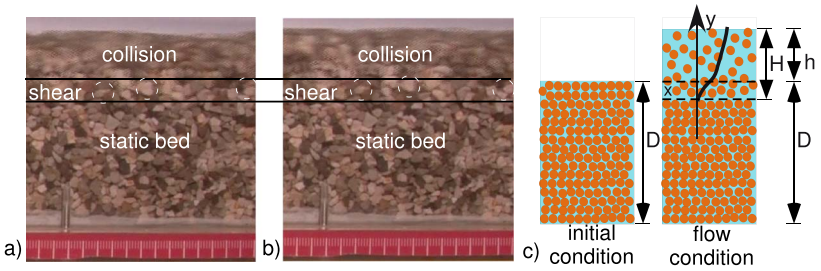

Figure 2. (a, b) Side view of typical mature flow conditions observed within the debris flow body at two successive instants, and sketch of the characteristic flow regimes occurring along the mixture column. (c) The flow depth h was measured with respect to the initial elevation of the sediment bed; the quantity H is the distance from the free surface to the point at which the local velocity u becomes about 1% of that at free surface.

component $\langle v_p \rangle$ tends to vanish, and the fluctuations $v'_p = v_p - \langle v_p \rangle$ attain values similar to $\langle v_p \rangle$, which, in turn, is 1 to 2 orders of magnitude smaller than $\langle u_p \rangle$. Tests carried out by injecting small air bubbles in the flow, and following bubble and grain trajectories from video records, indicated that sediment concentration was such that the velocity u_s of the solid phase and that of the interstitial fluid, u_f, are almost equal.

Two different flow depths have been computed (error $\pm d_s/2$) to characterize the flow in the body (Figure 2c): the depth h with respect to the initial bed surface, and the distance H from the free surface to the point at which the velocity u becomes negligible (1% of that at free surface). The depth h was obtained by averaging over time the free surface elevation during the passage of the body and subtracting from this value the initial elevation of the static bed. The depth-averaged debris flow velocity has been computed as $U = \int_0^h u(y)\mathrm{d}y$. The speed U_f of the debris flow front was also evaluated, by considering the position reached by the front at different times as resulting from video records.

The transport (bulk) sediment concentration C was estimated as the mean of two samples of material collected at the downstream end of the flume during the passage of the debris flow body. A bucket was placed at the flume outlet and the entire flow was intercepted. The sample was then weighted before and after removing the water. The weights were subsequently transformed in volumes by accounting for sediment and water densities. Finally, the bulk sediment concentration (error ±0.5%) was computed as $C = V_s/(V_s + V_f)$, where V_s and V_f are sediment and water volumes, respectively.

The solid discharge was calculated by considering the rate of change of the weight measured by the strain gauge applied to the large permeable collector placed under the flume outlet (Figure 1a), intercepting the sediment-water mixture mobilized by the debris flow. The signal measured by the strain gauge (sampling frequency 5 Hz) is given by the sum of the weights of the permeable collector, the trapped sediment, and the water contained in the pores of the solid matrix, and by the contribution due to the dynamic impact of the inflowing mixture. At two nearby instants, however, the rates of change of the dynamic impact and of the water weight are much smaller than that due to the deposited material, owing to the small variations in the area of the deposit, the large permeability of both the collector and the deposited sediment, and the small ratio of deposit thickness to deposit width. Hence, the slope of the recorded signal can be taken as representative of the solid discharge in weight. The volumetric discharge Q_S was eventually estimated by dividing this weight by the sediment density. The overall correspondence of the measured solid discharge was checked through a comparison with the quantity $U\,B\,h\,C$, or $U_f BCh$ in the absence of detailed measurements of the velocity profile (see supporting information S1). All the data collected during the experiments are reported idigitally in the supporting information file S2.

2.3. Flow Regimes

Three different flow regimes were attained in the tests (Figure 3): (i) immature debris flow, (ii) mature debris flow, and (iii) mature-accelerated (sliding) debris flow. Immature conditions were attained at lower slopes (10–14° for gravel, and 7–8° for glass spheres). The flow was not able to spread the sediment throughout the entire flow depth, and a distinct layer of clear water formed upon a flowing sediment-water mixture. Mature debris flow conditions (Figure 4) were observed for intermediate slopes (16–19° for gravel and 9–12° for glass spheres). This regime was invariably characterized by the formation of the following: a front, moving at an almost constant speed; a body of nearly constant depth, entailing a negligible erosion of the underlying

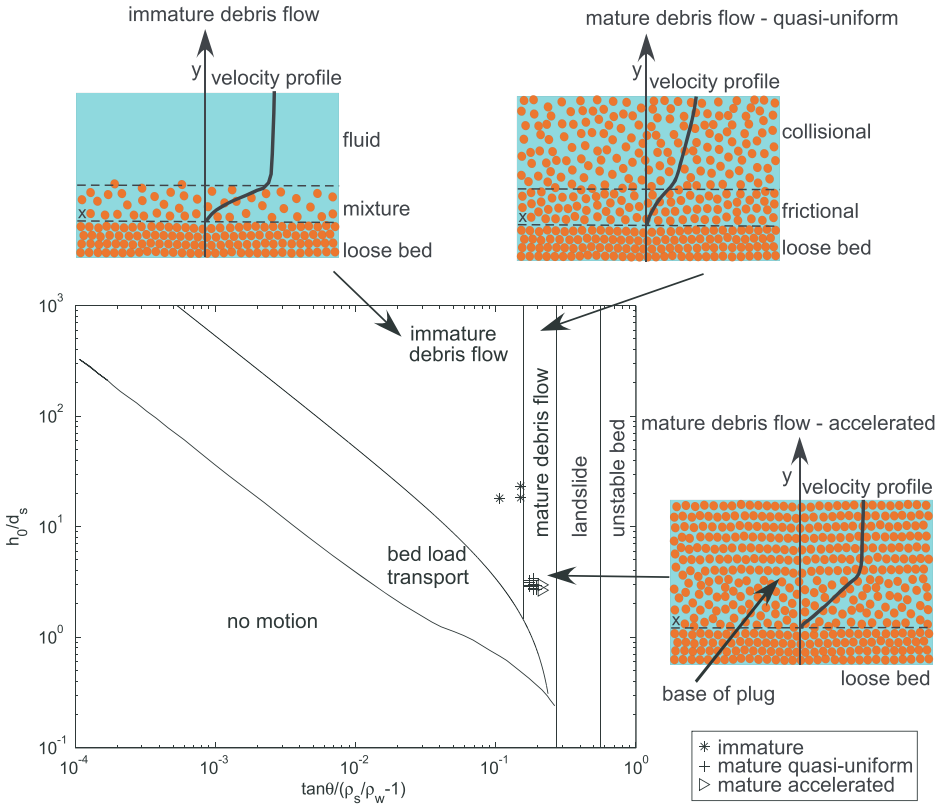

Figure 3. Sketch of the possible flow regimes and occurrence criteria [*Takahashi*, 2007] for a noncohesive coarse sediment bed. Tests carried out with 3 mm gravel.

sediment bed, that progressively elongates in time owing to sediment erosion in the upstream portion of the flume; and a tail where the entrainment of grains from the erodible bed is mainly concentrated. Accelerated debris flow conditions occurred at high enough values of the slope ($\gtrsim$19° for gravel and $\gtrsim$12° for glass spheres). Under these conditions, the saturated debris bed became almost unstable and the flow was not able to reach a quasi-equilibrium configuration because of the progressive increasing of flow depth due to the continuous entrainment of bed material. The consequent unsteadiness of the flow prevented the measurement of the velocity profiles. In the rest of the paper we will focus our attention on the mature debris flow regime.

3. Results

3.1. Overall Flow Features

Under mature debris flow conditions, for given bed slope and material, the depth-averaged flow velocity U is found to increase with Q_T at a higher rate than the flow depth h, while the bulk sediment concentration

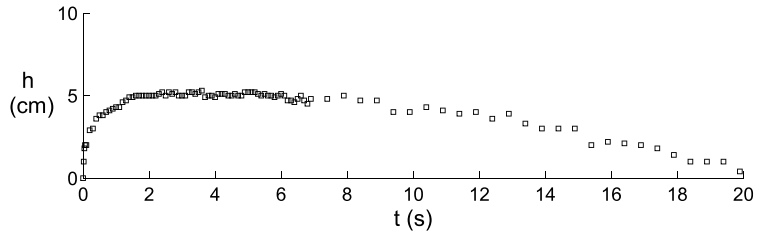

Figure 4. Temporal evolution of the debris flow surface elevation h, measured with respect to the initial elevation of the sediment bed. The data have been observed in section II and refer to run 60, carried out with 3 mm gravel, a slope angle of 17°, and a triggering discharge Q_T = 1.4 l/s. A higher sampling frequency has been chosen for the front and the body to capture the initial rapid increase of the flow depth and to better document the quasi-steady condition that establishes during the passage of the body.

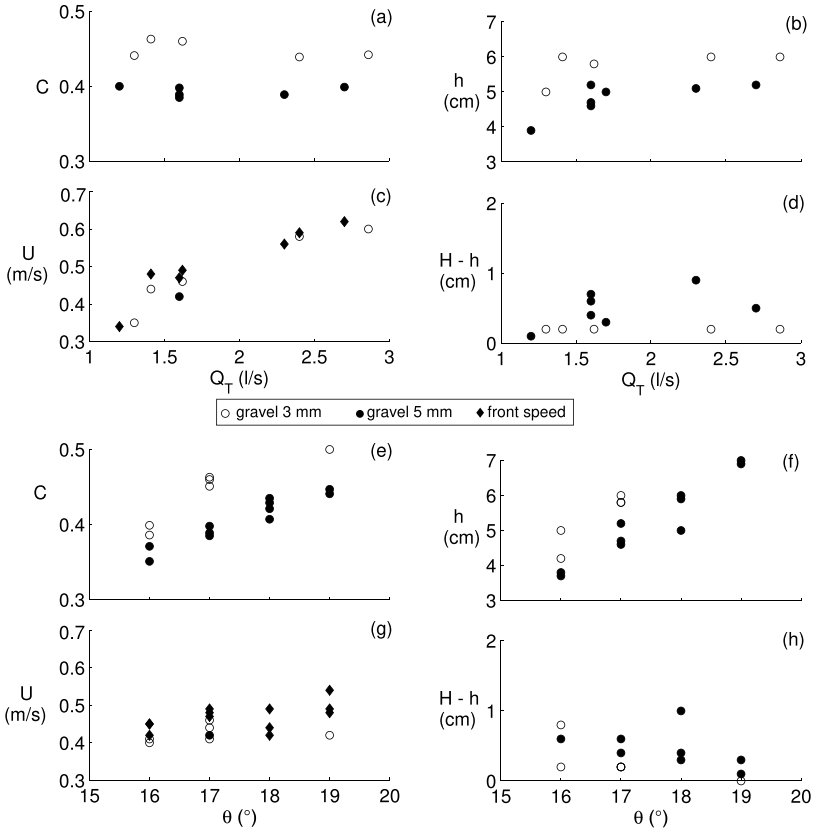

Figure 5. (a) Bulk sediment concentration C, (b) flow depth h (see Figure 2c), (c) depth-averaged debris flow velocity U and front speed U_f are plotted versus the triggering water discharge Q_T for a given slope angle (17°) and crushed gravel, (d) difference H-h (see Figure 2c). (e–h) The same quantities but for a variable slope angle θ and a given triggering discharge (~ 1.6 l/s).

C remains nearly constant (Figures 5a–5c). The experiments also indicate that for uniform sediments with similar particle shapes (e.g., crushed gravel), increasing the grain size leads to an overall decrease of C and h, while the variations of U remain relatively limited. In other words, sediment size, more than water discharge, likely controls the flow depth and sediment concentration, all the other experimental conditions being the same. The increase of sediment entrainment rate associated with a larger triggering discharge determines a higher front speed and a lengthening of the debris flow body, rather than an increase in flow depth, without influencing significantly the bulk concentration. Slightly different trends are observed by fixing the triggering discharge and varying the bed slope: specifically, C, h, and, to a lesser extent U, increase as θ (Figures 5e–5g). Finally, we note that the speed of the debris flow front U_f almost coincides with the depth-averaged velocity U (Figures 5c and 5g).

3.2. Velocity Profiles

Figure 2 illustrates the flow characteristics typically observed inside the body of the debris flow. The high solid concentration throughout the flow depth inhibits particle displacements normal to the bed, as suggested by the vanishing values attained by the v component of the velocity (see supporting information S1). Near the bed, particles tend to move by layers, rolling and rubbing on contiguous layers, implying the dominance of frictional (quasi-static) stresses that are transmitted through the skeletal structure. At the interface between this layer and the underlying static bed, the flow velocity tends to zero with a tangent almost normal to the flow direction and the particle concentration tends to equal the maximum packing value, C_{max}. In the upper flow region, where the interparticle distance increases, particle collisions prevail, leading to a nearly linear profile. The relative thickness of these upper and lower flow layers depends on sediment characteristics and channel slope, and influence the overall distributions of velocities and concentration along the flow depth.

Figure 6 shows some representative examples of the velocity profiles observed in the cases of 3 mm gravel (Figure 6a) and glass spheres (Figure 6b). The plots report the single grain velocities, the layer-averaged

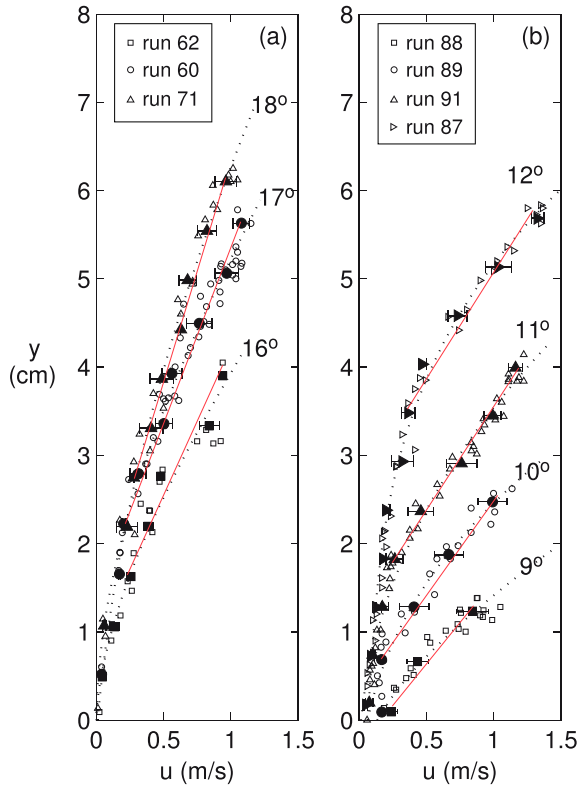

Figure 6. Typical velocity profiles observed at different channel slope angles for a similar triggering discharge: (a) 3 mm gravel; (b) 3 mm glass spheres. White symbols denote single-particle velocities; black symbols refer to binned velocities; horizontal bars represent the standard deviation within a given bin; dotted lines represent the least squares fitting made with a third degree polynomial; red lines denote the upper portion of the observed profile that can be approximated as almost linear.

(binned) values, and the corresponding standard deviation bars. In general, the profiles are characterized by an upper region (of thickness ~5–10 d_s) exhibiting an almost linear behavior, and a lower region (of thickness ~4–7 d_s) with a down oriented concavity, tangent to the normal to the flow (see also the individual profiles reported in the supporting information S1). Most of the profiles show a gradual transition from the lower region to the upper region. Overall, these trends agree with the flume observations made by *Armanini et al.* [2005, 2009] for mature and uniform debris flow conditions. A concave down lower profile, associated with the presence of a movable bed, has also been documented in the rotating drum tests of *Kaitna et al.* [2014, 2016]. The difference $H - h$ between the distance from the free surface at which the velocity becomes negligible and the flow depth estimated with respect to the initial bed level is, in general, of the order of a few particle grains (see Figures 5d, 5h, and Tables 1–3 of the supporting information S1), thus indicating negligible erosion of the initial static bed during the passage of the debris flow body. On the other hand, the thickness of the upper layer where the velocity exhibits a nearly linear behavior is invariably smaller than h (see the individual velocity profiles reported in the supporting information S1).

For a given material and similar triggering discharges, the shape of velocity profiles varies according to the bed slope (Figure 6). The data shown in Figures 5b and 5c indicate that, for a fixed slope, the depth-averaged velocity U is remarkably influenced by the triggering discharge, while the flow depth h undergoes a milder growth. In order to rule out the effects of runoff variations and different slopes, and investigate whether a self-similar shape does exist, the velocity profiles have been made dimensionless as shown in Figure 7.

The coordinate y has been scaled by either h or H, setting:

$$\hat{y} = \frac{y}{h}, \qquad \tilde{y} = \frac{y + H - h}{H} \tag{2}$$

Finite velocities occurring at negative values of $\hat{y}$ correspond to layers of the loose sediment bed where the overrunning debris flow gives rise to a slow frictional motion. On the other hand, the dimensionless variable $\tilde{y}$,

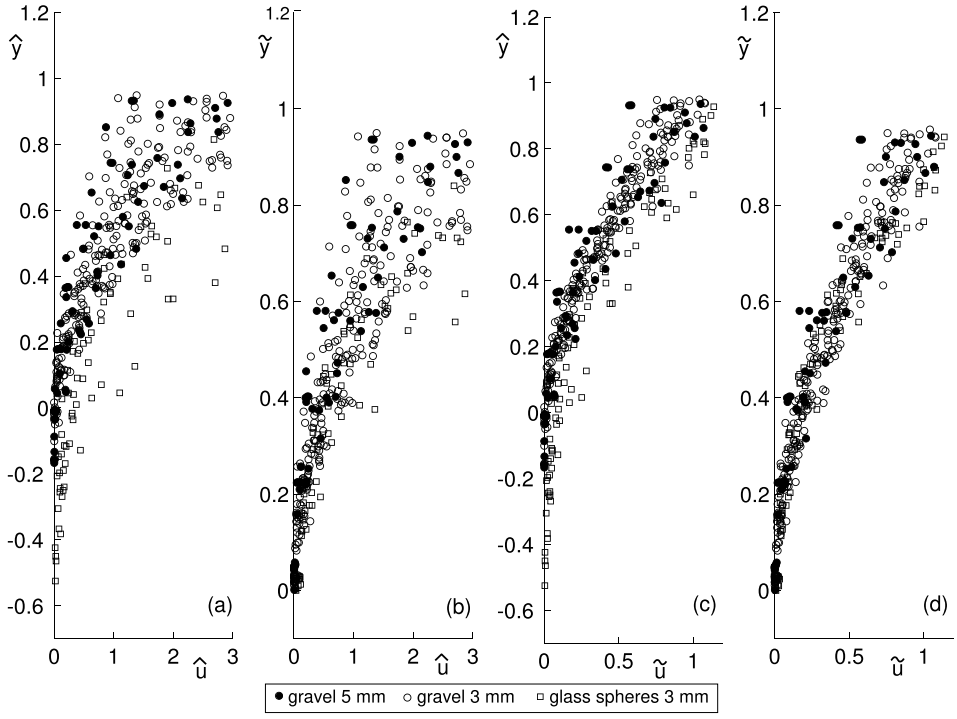

Figure 7. Dimensionless velocity profiles observed in the flume tests. The coordinate y normal to the bed has been normalized either as (a, c) $\hat{y} = y/h$ or (b, d) $\tilde{y} = (y + H - h)/H$. The velocity u has been scaled as either $\hat{u} = u/\sqrt{gh \sin\theta}$ (Figures 7a and 7b) or $\tilde{u} = u/U_0$ (Figures 7c and 7d). Here h is the flow depth with respect to the initial elevation of the static bed; H denotes the distance from the free surface to the point at which u is ~1% of that at free surface; U_0 is the runoff velocity defined by equation (1).

implying a common zero velocity, can reveal the existence of self-similar profiles. In order to evaluate this possibility, two different normalizations have been considered for the velocity, namely:

$$\hat{u} = \frac{u}{\sqrt{gh \sin\theta}}, \qquad \tilde{u} = \frac{u}{U_0} \tag{3}$$

The first ($\hat{u}$) accounts for the friction velocity $u_* = \sqrt{gh \sin\theta}$, which corresponds to the gravity-driven velocity scale $\sqrt{gh}$, corrected for bed slope. The resulting dimensionless profiles, however, turn out to be spread out (Figures 7a and 7b) as a consequence of the high sensitivity of mean flow velocity to the triggering discharge (Figure 5c). The second normalization ($\tilde{u}$), based on the runoff velocity U_0, accounts for variation of U with Q_T. The resulting dimensionless profiles exhibit a remarkable degree of similarity (Figures 7c and 7d). This result emphasizes the important role that runoff discharge can have in destabilizing the loose sediment on scree slopes and in spreading them throughout the entire flow depth, eventually influencing the mean velocity of the solid-liquid mixture and, to a less extent, the flow depth.

4. Discussion

4.1. Dynamic Similarity

The use of laboratory data is typically limited by scaling problems resulting from the relatively small size of experimental setups. Dynamic similarity of experimental and full-sized debris flows require that the relevant dimensionless parameters have the same values in the prototype and in the model, assumed to be geometrically similar. Nevertheless, as it often occurs also in hydrodynamic problems, such a full similarity can be attained only for a relatively small geometric reduction scale and, hence, requires large enough scale models. In addition, many processes (shear stress generation by grain collisions, grain contact friction, viscous and turbulent fluid shear, and solid-fluid interactions) determine the overall rheological behavior of the mixture and, consequently, its dynamics. In examining the experimental results, we then have to evaluate the presence of possible scale effects associated with the reduced geometrical scale and the difficulty to reproduce correctly the relative importance of differently generated stresses.

In general, five types of stresses control the dynamics of a sediment-water mixture [*Iverson*, 1997; *Takahashi*, 2007]: the inertial and quasi-static stresses associated to collisions ($T_i^{(s)}$) and long-lasting contacts ($T_q^{(s)}$) of sediment grains; the turbulent ($T_t^{(f)}$) and viscous ($T_v^{(f)}$) fluid stresses; and the interaction stresses ($T^{(s-f)}$) associated with the relative fluid-grain motion. The relative influence of the physical mechanisms determining these stresses can be accounted for through the following dimensionless groups:

$$N_{Sa} = \frac{T_i^{(s)}}{T_q^{(s)}} = \frac{\rho_s d_s^2 \dot{\gamma}^2}{\sigma_e}, \quad N_{Ba} = \frac{T_i^{(s)}}{T_v^{(f)}} = \frac{\lambda^{1/2} \rho_s d_s^2 \dot{\gamma}}{\mu_f},$$

$$N_m = \frac{T_i^{(s)}}{T_t^{(f)}} = \frac{C \rho_s}{(1-C)\rho_f}, \quad N_{Da} = \frac{T_i^{(s-f)}}{T_i^{(s)}} = \frac{\mu_f}{C \rho_s k \dot{\gamma}},$$

$$N_f = \frac{T_q^{(s)}}{T_v^{(f)}} = \frac{N_{Ba}}{N_{Sa}}, \quad N_{Re} = \frac{T_t^{(f)}}{T_v^{(f)}} = \frac{N_{Ba}}{N_m}.$$

where N_{Sa} is the Savage number [*Savage and Hutter*, 1989], N_{Ba} is the Bagnold number [*Bagnold*, 1954], N_m is the mass number [*Iverson and Vallance*, 2001], N_{Da} is the Darcy number [*Iverson*, 1997], N_f is the friction number [*Iverson*, 1997], and N_{Re} is the Reynolds number [*Iverson*, 1997]. The macroscopic flow quantities used to estimate these dimensionless groups are the shear rate, $\dot{\gamma} = \mathrm{d}u/\mathrm{d}y$; the effective normal basal stress, σ_e; the size and density of sediment particles, d_s and ρ_s; the viscosity and density of the interstitial fluid, μ_f and ρ_f; the bulk sediment concentration, C; the linear concentration, $\lambda = C^{1/3}/(C_{\max}^{1/3} - C^{1/3})$; and the hydraulic (intrinsic) permeability of the coarse sediment matrix, k.

Depending on the values attained by these dimensionless numbers, the debris flows have been classified [*Takahashi*, 2007] as either quasi-static (small N_{Sa} and N_m) or dynamic (large N_{Sa} and N_m). On the other hand, three types of dynamic debris flows can exists: stony debris flows, dominated by grain collision stresses (large N_{Ba}); turbulent-muddy debris flows, controlled by turbulent mixing stresses (large N_{Re}); and viscous flows, dominated by viscous stresses (small N_{Ba} and N_{Re}). In general, small values of N_{Sa} and N_{Ba} indicate that collision stresses are negligible, whereas friction and viscosity dominate. Large values of N_f suggest that frictional shear stresses tend to exceed viscous shear stresses. Large values of N_{Da} and small values of N_{Re}, indicate that viscous drag associated with solid-fluid interactions is likely to be important.

The Darcy number describes also the tendency of pore fluid pressure developed between moving grains to damp grain collisions. In particular, significant departures p_b' ($= p_b - \rho_f g h \cos\theta$) of the basal pore fluid pressure p_b from the hydrostatic distribution ($= \rho_f g h \cos\theta$) are expected only for high values of the relative volumetric flux (proportional to $u_s - u_f$) of the pore fluid. In the presence of a relatively coarse debris matrix and a sufficiently diluted interstitial slurry (i.e., for a moderate content of fines), a rapid dissipation of excess pore fluid pressure likely occurs [*Hotta*, 2012; *Stancanelli et al.*, 2015; *Kaitna et al.*, 2016]. It is also interesting to note that, if viscous drag dominates (as, for example, in the case of submarine avalanches of fine sediments occurring over a continental margin), the Savage number has to be suitably modified. Indeed, N_{Sa} is equivalent to the square of the inertial number I introduced by *GDRMiDi* [2004] for dry granular flows and can be interpreted as the ratio of the timescale of particle rearrangements under the action of the confining pressure, $t_p = d_s/\sqrt{\sigma_e/\rho_s}$, to the timescale $t_{\dot{\gamma}} = 1/\dot{\gamma}$ associated with particle shearing [*da Cruz et al.*, 2005].

The relevant dimensionless groups introduced above can help in evaluating the importance of possible scale effects. To this aim we analyzed the data collected for a number of debris flows observed in different field sites (Table 2). The bulk sediment concentration data for the Illgraben, Moscardo, and Yakedake field sites are those reported in the cited literature, while those corresponding to Acquabona, Chalk Cliff, and Houyenshan sites have been estimated from the bulk mixture density and the fluid density data reported by the various authors. All the monitored debris flows consisted of a coarse solid matrix, made by sediment ranging from gravel (0.002–0.064 m) to cobbles (0.064–0.256 m) and boulders (> 0.256 m), and an interstitial slurry. The density ρ_f and the viscosity μ_f of this slurry depend on the percentages of the fine sediment fractions mixed in it. The slurry density can thus vary from that of water (1000 kg/m^3) if silt and clay fractions are negligible, to values larger than 2000 kg/m^3 in the presence of fines made by 100% of silt and clay [*Parsons et al.*, 2001]. Similarly, the slurry viscosity can vary from 0.002 to 0.06 Pa s, for mixtures composed mainly of sand, to 0.5–1 Pa s for mixtures in which fines ($d_s < 0.064$ m) prevail, and increases substantially in the presence of

clay [*Parsons et al.*, 2001; *Cui et al.*, 2015]. It is much more difficult to estimate the hydraulic permeability k needed to compute the Darcy number. This quantity may vary by more than an order of magnitude [*Major*, 2000]. As a first rough approximation, k can be related to the porosity ϕ of the sediment mixture by means of the fractional packing Kozeny-Carman equation [*Koltermann and Gorelick*, 1995]:

$$k = \frac{d_s^2 \phi^3}{180 (1-\phi)^2} \tag{4}$$

where the grain size d_s is taken to represent the coarse debris matrix, and the porosity is computed by considering the fractional packing model:

$$\phi = \phi_c - r_\phi C_f \left(1 - \phi_f\right) + \left(1 - r_\phi\right) C_f \phi_f \tag{5}$$

Here ϕ_c and ϕ_f are the porosities of the coarse ($d_s \geq 0.064$ m) and fine ($d_s < 0.064$ m) grain components of the sediment mixture, C_f is the volume concentration of the fine-grained fractions, and r_ϕ is a coefficient that reflects the relative proportions of coarse and fine packing, varying from a maximum of 1 (no fine grains in the mixture) to a minimum $r_{\phi_{\min}}$ ($r_{\phi_{\mathbf{min}}} > 0$) when the volume fraction of fines equals the porosity of the coarse grain component. For the materials adopted in the present tests, k is of the order of 10^{-9} m^2, with an average value of 7×10^{-9} m^2, while for the observed field events the estimates of k resulting from this methodology are reported in Table 2.

The graphical representation of the six-dimensional parameter space defined so far has many degrees of freedom. Here we choose to represent together N_{Ba} and N_{Sa}, given the various classifications of rheological regimes proposed in terms of these two numbers [*Iverson*, 1997; *GDRMiDi*, 2004; *Armanini et al.*, 2005; *Takahashi*, 2007]. We grouped together N_{Re} and N_f, since they both involve the viscous fluid stresses. Finally, we plotted N_{Da} and N_m as a function of the bulk concentration C that appears explicitly in the expressions of these two numbers. Figure 8 shows the distribution of the present experimental data in the planes (N_{Sa}, N_{Ba}), (N_f, N_{Re}), (C, N_m), and (C, N_{Da}), as compared to the points representative of real debris flows. In both cases, the shear rate $\dot{\gamma}$ needed to compute the dimensionless groups has been estimated as the ratio of free surface velocity (or front velocity, depending on the available data) to flow depth. For flume experiments, estimates of N_{Sa}, N_{Ba}, N_f, N_{Re}, and N_{Da} have been provided also computing $\dot{\gamma}$ in the lower, frictional part of the flow, fitting with a straight line the velocity profiles observed in this region.

In general (Table 3), the values of the dimensionless numbers characterizing the present flume tests are compatible with those computed for the full-size debris flows listed in Table 2. Figure 8a suggests that a collisional regime ($N_{Sa} > 0.1$ and $N_{Ba} > 450$) prevails in the laboratory-generated debris flows and in those observed at Acquabona, Chalk Cliff, Moscardo, and Yakedake. Note that the flume values of $\hat{u}$ are similar to those observed by *Suwa et al.* [2011] for the stony debris flows that occurred in the Kamikamihori gully. Conversely, the events monitored at Houyenshan and Illgraben tend to fall in the frictional dominated region. Note also that according to *Armanini et al.* [2005], the transition from a frictional to a collisional behavior is controlled by the viscosity of the interstitial fluid and occurs for $N_{Ba} \sim 1000$.

Overall, the cluster of points associated with Acquabona, Moscardo, and Yakedake debris flows tend to be slightly shifted toward larger N_{Ba} and smaller N_{Sa} with respect to the points characterizing flume tests. On the other hand, the points representing the Illgraben and Houyenshan events tend to overlap to those computed considering the shear rate in the lower, frictionally dominated layer of flume tests (gray area in Figure 6). The scenario emerging from the (N_{Sa}, N_{Ba}) plot is substantially confirmed by the data reported on the (N_f, N_{Re}) plane (Figure 8b). The points corresponding to Acquabona, Moscardo, and Yakedake are on average characterized by larger values of N_{Re}, while those referring to Illgraben and Houyenshan correspond to a stress regime dominated by viscous and quasi-static actions, similarly to the frictionally dominated layer of flume experiments (gray areas in Figure 8). The points corresponding to Chalk Cliff overlie those observed in flume tests.

Also, the ranges of values attained by the mass number and the Darcy number in flume tests (Figure 8c) are similar to those observed in the field. The values of N_m, typically greater than 1, suggest that momentum transport is dominated by solid grain dynamics and that an increase of sediment concentration results in an increase of N_m. Finally, the range of variation of N_{Da} is definitely quite large, given the uncertainties embodied by the estimate of the hydraulic permeability. Nevertheless, the relatively small values of N_{Da} typical of

Table 2. Typical Values of Debris Flow Properties Observed in Different Field Sites[a]

Site	d_s (mm)	h (m)	U_f (m/s)	θ (deg)	C	ρ_f (kg/m^3)	μ_f (Pa s)	k (m^2)
Acquabona[b]	258	1.2	1.2	16	0.30	1200	0.1	$4.52 \cdot 10^{-6}$
		1.4	7.7					
Chalk Cliffs[c]	114	0.3	1.3	20	0.51	1100	0.1	$2.16 \cdot 10^{-6}$
Houyenshan[d]	100	1.3	1.5	11	0.35	1050	0.1	$1.23 \cdot 10^{-7}$
Illgraben[e]	50	1.1	2.4	10	0.40	1200	0.1	$2.06 \cdot 10^{-7}$
		2.4	5.5					
		1.5	1.9					
Moscardo[f]	400	3.0	3.2	14	0.30	1100	0.1	$6.00 \cdot 10^{-6}$
		3.8	4.0					
		4.0	2.9					
		1.6	9.4					
		2.0	7.9					
		1.1	3.0					
Yake Dake[g]	290	0.5	0.9	9	0.40	1250	0.1	$3.56 \cdot 10^{-6}$
		1.7	4.3					
		4.2	4.3					
		3.2	3.7					
		2.0	1.9					
		2.8	1.9					
		4.2	4.4					
		2.8	1.8					
		4.3	4.2					
		1.4	0.6					
		1.7	1.8					
		1.7	2.3					
		2.9	2.9					
		3.9	3.5					

[a] d_s, Grain diameter representative of the coarse sediment matrix; h, flow depth; U_f, front velocity; θ, slope angle; C, volume sediment concentration; ρ_f, interstitial fluid density; μ_f, interstitial fluid viscosity; k, hydraulic permeability. Given the relatively small range of variation, a sediment density of 2650 kg/m^3 has been assumed for all field sites. In the absence of specific information, we set $C_{max} = 0.65$.
[b] Acquabona basin, Italy [*Berti et al.*, 1999, 2000].
[c] Chalk Cliff, Central Colorado, USA [*Coe et al.*, 2008; *McCoy et al.*, 2010, 2013].
[d] Houyenshan ravine, Taiwan [*Chou et al.*, 2013].
[e] Illgraben catchment, Switzerland [*Badoux et al.*, 2008; *Berger et al.*, 2011; *Bennett et al.*, 2014].
[f] Moscardo Torrent, Italy [*Marchi et al.*, 2002; *Arattano and Franzi*, 2004].
[g] Kamikamihori gully, Yake Dake, Japan [*Takahashi*, 2007; *Suwa et al.*, 2009; *Okano et al.*, 2012].

present tests suggests that a rapid dissipation of excess pore fluid pressure likely occurs, owing to the complete absence of fine sediment mixed in the interstitial fluid [*Hotta*, 2012; *Stancanelli et al.*, 2015; *Kaitna et al.*, 2016]. This conjecture is confirmed by the analysis of the Stokes number N_{St}, measuring the importance of the fluid drag, proportional to $(u_s - u_f)^2$, which can arise in the presence of a nonnegligible relative motion of the solid-liquid phases. This number is defined as

$$N_{St} = \frac{t_{av}}{t_{ai}} = \frac{\alpha d_s \sqrt{\rho_s 2\sigma_e/3}}{\mu_f}, \tag{6}$$

where t_{av} is the time of deceleration due to Stokes viscous drag force, t_{ai} is the time needed for a particle to move a distance of one grain size through the liquid, and α is a coefficient that depends on the size distribution

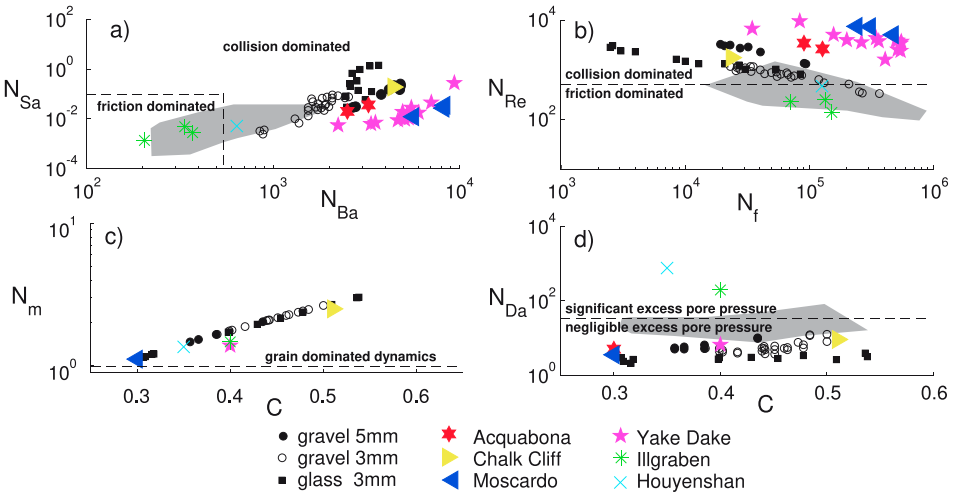

Figure 8. The experimental data of *Lanzoni* [1993] are plotted in the parameter spaces (a) (N_{Sa}, N_{Ba}), (b) (N_f, N_{Re}), (c) (C, N_m), and (d) (C, N_{Da}), together with the data referring to a number of debris flows observed in different field sites (Table 2). In both cases, the velocity shear rate $\dot{\gamma}$ needed to compute the various dimensionless groups has been estimated as the ratio of free surface velocity (or front velocity, depending of the available data) to flow depth. The area delimited by dashed lines in Figure 8a corresponds to the region $N_{Ba} < 450$, $N_{Sa} < 0.1$, where long-lasting solid friction and fluid viscosity dominate while collisions transmit negligible stresses. Dashed lines mark the different rheological regimes also in Figures 8b–8d. The gray areas refer to values of the dimensionless numbers for which $\dot{\gamma}$ has been computed with reference only to the lower, frictional part of the velocity profiles observed in present flume tests.

of particles and the deformation of the mixture [*Cassar et al.*, 2005]. For the present flume experiments, N_{Sa} fall in the range 11–48. These values, being much larger than one, indicate a negligible fluid drag action.

In summary, the values attained by the Stokes number and the Darcy number (in the range 2.1–12.7) suggest that excess pore pressure dissipates quite rapidly in the present tests and, possibly, in a number of debris flows (e.g., Acquabona, Yake Dake, Chalk Cliff, and Moscardo) observed in the field for a quite coarse debris matrix and a moderate content of fines. Note that, in the debris flow body, where nearly uniform flow conditions occur, a hydrostatic distribution of the interstitial fluid pressure is in any case expected owing to the balance in the fluid phase between the gravitational force and the pressure gradient in the direction normal to the flow [*Armanini et al.*, 2014]. Clearly, for mixtures with high fraction of fines ($N_{Da} \gg 50$–60) excess pore fluid pressure is significant, and can lead to lower values for the bulk flow resistance, damped fluctuations of normalized fluid pressure and normal stress, velocity profiles with the shear concentrated at the base of the flow [*Kaitna et al.*, 2016], and enhanced run out [*de Haas et al.*, 2015].

4.2. Role of Quasi-Static Stresses

The measurements of the bulk sediment concentration C can be used for assessing the role of quasi-static stresses in the region close to the underlying static sediment bed. Assuming that C, measured in bulk at the flume outlet, approximates the depth-averaged concentration and that a frictional behavior dominates at the base of the flowing layer [*Armanini et al.*, 2005; *Larcher et al.*, 2007], the ratio of the basal bed shear stress τ_0 to the basal confining normal pressure σ_e reads:

$$\frac{\tau_0}{\sigma_e} = \frac{[(\rho_s - \rho_f)\int_0^h c\,dy + h\,\rho_f]\,\sin\theta}{(\rho_s - \rho_f)\int_0^h c\,dy\,\cos\theta - p_b'/g} = \tan\varphi_{qs} \tag{7}$$

with c the local concentration. Figure 9 shows the values of τ_0/σ_e, computed by neglecting the excess basal pore fluid pressure p_b' on the basis of the results discussed in section 4.1 and assuming that $\int_0^h c\,dy \sim Ch$. The data suggest that, for a given material, the ratio τ_0/σ_e (and hence $\tan\varphi_{qs}$) does not depend on N_{Sa} and N_{Ba}, in accordance with the findings of *Bagnold* [1954] and *Kaitna et al.* [2014]. In the case of crushed gravel, the corresponding values of φ_{qs} (Table 1) are invariably smaller than their static counterparts φ_s. A much more scattered trend is observed for the cylinder-shaped PVC pellets used by *Armanini et al.* [2005] (Figure 9). In this case $\varphi_{qs} = 34.6^o$ as compared to the value 31.0° obtained by simple shear tests. On the other hand, in the case of glass spheres the enhanced sliding mobility ensured by particle shape tends to homogenize the values

Table 3. Typical Values of the Relevant Dimensionless Parameters Defined in Section 4.1[a]

Source	N_{Ba} $\times 10^3$	N_{Sa} $\times 10^{-1}$	N_f $\times 10^4$	N_{Re} $\times 10^4$	N_{Da}	N_m	C
Gravel A[b]	2.7–4.8	0.3–2.5	1.9–9.4	0.13–0.33	5.1–10.1	1.47–2.04	0.35–0.45
Gravel B[b]	0.8–2.5	0.02–0.9	2.3–36.7	0.03–0.12	3.7–12.7	1.66–2.65	0.39–0.50
Glass spheres[b]	0.2–3.7	0.01–14.0	1.4–8.5	0.08–0.31	2.1–4.0	1.15–3.03	0.31–0.54
Acquabona[c]	2.5–17.9	0.2–9.3	1.9–12.8	0.26–1.89	1.69	0.95	0.30
Chalk Cliffs[d]	4.4	1.9	2.4	0.18	9.22	2.51	0.51
Houyenshan[e]	0.6	0.05	12.7	0.05	760	1.36	0.35
Illgraben[f]	0.2–0.4	0.01–0.04	7.1–15.2	0.01–0.02	65.2	1.47	0.40
Moscardo[g]	5.7–45.9	0.1–19.6	2.3–47.4	0.51–4.13	0.59	1.11	0.30
Yake Dake[h]	2.2–13.2	0.05–2.7	3.5–55.1	0.16–0.95	0.47	1.39	0.40
USGS large flume[i]	1.6	0.2	9.5	0.04	617	3.68	0.600
rotating drum[j]	11.1	0.3	33.8	0.34	67	3.23	0.550
runout tests[k]	0.3	0.7	0.38	0.01	3.4×10^6	2.0	0.490

[a]For the Bagnold number, in the absence of specific information, we set $C_{max} = 0.65$.
[b]Present flume experiments [*Lanzoni*, 1993].
[c]Acquabona basin, Italy [*Berti et al.*, 1999, 2000].
[d]Chalk Cliff, Central Colorado, USA [*Coe et al.*, 2008; *McCoy et al.*, 2010, 2013].
[e]Houyenshan ravine, Taiwan [*Chou et al.*, 2013].
[f]Illgraben catchment, Switzerland [*Badoux et al.*, 2008; *Berger et al.*, 2011; *Bennett et al.*, 2014].
[g]Moscardo Torrent, Italy [*Marchi et al.*, 2002; *Arattano and Franzi*, 2004].
[h]Kamikamihori gully, Yake Dake, Japan [*Takahashi*, 2007; *Suwa et al.*, 2009; *Okano et al.*, 2012].
[i]USGS, large scale debris flow experiment [*Iverson*, 1997].
[j]Rotating drum experiment, water, and gravel 10 mm, [*Hsu et al.*, 2008].
[k]Runout tests (grain size distribution experiment no. 36 in the supporting information of *de Haas et al.* [2015]).

of φ_{qs} and φ_s (Table 1). The possible departure of φ_{qs} from the static friction angle then seems to depend on the type and shape of material. In the case of cylinder-shaped pellets, however, the scatter could be also partly due to the different procedure used to generate the debris flow, based on recirculating a prescribed solid-liquid discharge.

These results reflect the crucial role that quasi-static stresses and grain form can exert on the lower part of the velocity profiles and on the bulk volume concentration. Clearly, in order to obtain an a priori estimate of the concentration would require that φ_{qs} is determined independently of C. This can be done through separate measurements of the basal shear stress and confining pressure, not available for the present experiments. Anyway, equation (7) provides information on the scaling of C with bed slope and sediment characteristics. In the presence of a negligible excess basal pore fluid pressure, it can be rearranged in terms of C as

$$C = \frac{\rho_f \tan\theta}{(\rho_s - \rho_f)(\tan\varphi_{qs} - \tan\theta)}, \tag{8}$$

This relation is in accordance with that derived by *Egashira et al.* [1997], accounting for the contributions of inelastic collisions, hydrostatic fluid pressure, and Coulomb shear stress at the bed. Figures 10a and 10b shows the concentration corresponding to various experimental data sets [*Takahashi*, 1978; *Tsubaki et al.*, 1983;

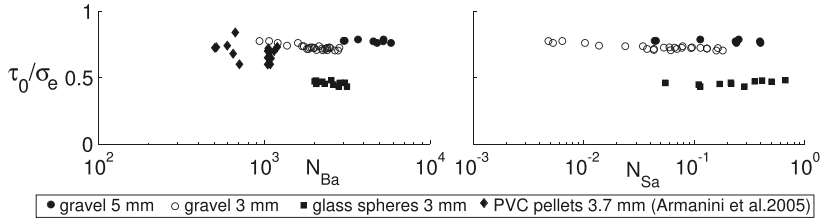

Figure 9. The values of τ_0/σ_e, computed according to equation (7), are plotted versus (left) N_{Ba} and (right) N_{Sa}. The data concerning cylinder-shaped PVC pellets are taken from *Armanini et al.* [2005].

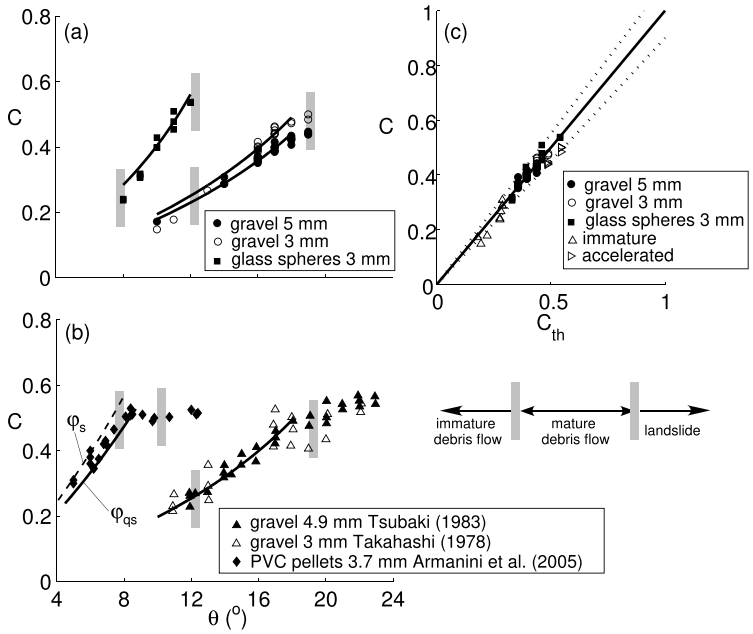

Figure 10. Measured mean sediment concentration C is plotted versus bed slope angle for (a) present experiments [*Lanzoni*, 1993] and (b) experiments carried out by *Takahashi* [1978], gravel 3 mm; *Tsubaki et al.* [1983], gravel 4.9 mm; *Armanini et al.* [2005], PVC pellets. The solid lines have been calculated through equation (8), using either the quasi-static friction angle φ_{qs}, if known, or the static friction angle φ_s. The vertical gray bars denote the upper and lower limit angles for the occurrence of mature debris flows estimated by *Takahashi* [1978]. (c) Comparison of the values of C observed in the present experiments with the values C_{th} computed by means of equation (8). The dotted lines denote ±10% errors.

Lanzoni, 1993; *Armanini et al.*, 2005]. The functional dependence of C from the slope angle described by equation (8) is evident for glass spheres and crushed gravel. On the other hand, a spurious relationship likely holds for PVC pellets, as suggested by the scatter of φ_{qs} observed in Figure 9.

In the case of present tests, the difference between the measured values of C and those resulting from equation (8) are mostly contained in the ±10% range (Figure 10c). The relatively larger scatter characterizing the data shown in Figure 10b and the absence of a clear dependence of C on the sediment grain size could be partly imputed to the different precision of the measurement systems employed in the different series of experiments. Moreover, owing to the absence of any information on φ_{qs}, the value given for φ_s (~36.5°) has been adopted in (8) when considering *Takahashi* [1978] and *Tsubaki et al.* [1983] data. We also observe that the points corresponding to immature debris flow conditions (on the left of the vertical bar defining the lower limit angle for mature flow conditions) tend to depart from theoretical predictions, while the accelerated sliding regime data typically exhibit an almost constant depth-averaged concentration, independently of the channel slope.

The picture emerging from Figure 10, involving flume tests carried out with different experimental procedures, different materials, and different ranges of the relevant parameters, is quite consistent and supports the functional dependence of C described by equation (8). In particular, it is worthwhile to observe that in the experiments carried out by *Takahashi* [1978], *Tsubaki et al.* [1983], and *Lanzoni* [1993], debris flows were triggered by releasing a preset water discharge at the upstream section of a flume filled by a preliminary saturated sediment bed. The debris flows studied by *Armanini et al.* [2005] were instead generated by recirculating prescribed solid and liquid discharges, eventually attaining uniform flow conditions and a well-defined value of the transport concentration. As thoroughly discussed in *Armanini et al.* [2005], recirculating the same amount of solid volume with different liquid volumes essentially corresponds to different bed slopes. Conversely, in Lanzoni's [1993] experiments, varying the upstream water discharge at a fixed bed slope does not lead to different values of C but rather affects the rate of entrainment and, hence, U, as discussed in section 2.1. This different behavior is possibly related to the different inertia initially characterizing the solid phase: in the case of a nonrecirculating flume it is zero, whereas it is imposed by the apparatus itself in the case of a recirculating flume. Moreover, the debris flows obtained by destabilizing a saturated sediment bed through runoff

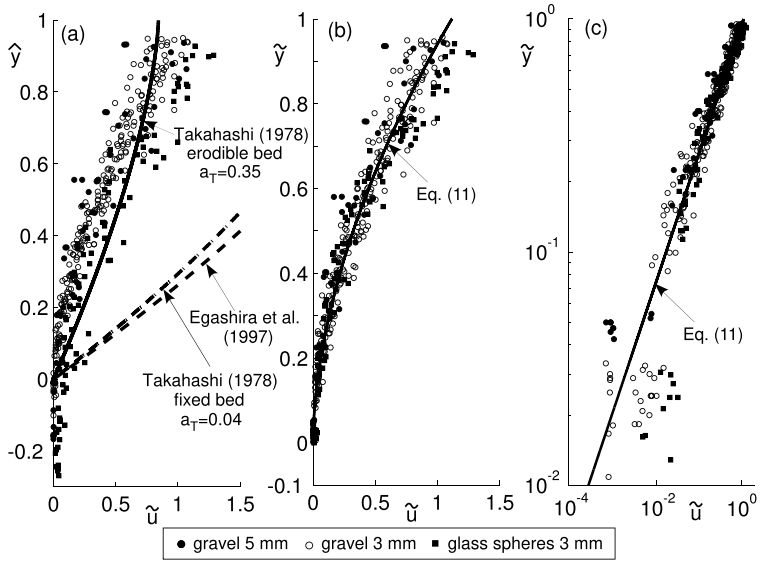

Figure 11. The observed dimensionless velocity profiles are compared with (a) three typical Bagnold-like profiles, computed for 3 mm gravel, $\theta = 17°$, $Q_T = 1.6$ l/s; (b,c) the profile provided by fitting equation (11) to the entire set of dimensionless profiles ($\beta = 1.79$, $k_0 = 1.11$).

discharge exhibits a relatively diluted tail following the body (see Figure 1), as it typically occurs in real debris flows. As a consequence, not all the supplied water discharge contributes to the debris flow body as it occurs in a recirculating system.

4.3. Coherence Length Approach

The considered flume data indicate that the velocity profiles observed in coarse-grained debris flow experiments are characterized by two regions with a generally smooth transition between them: a lower layer with a concave down velocity profile, tending asymptotically to vanish at the interface with the static sediment bed; and an upper layer where the velocity distribution can be approximated as rectilinear (Figures 6 and 7). This latter feature is a further evidence that in this upper layer both collisional and frictional stresses likely contribute to determine the mixture rheology. A pure collisional regime would in fact imply a rheological relation of the form $\tau/\sigma_e = f(I) = \tan\varphi_{qs}$, that yields the Bagnold-like velocity profile

$$\tilde{u} = \mathcal{A}\left[1 - (1-\hat{y})^{3/2}\right], \tag{9}$$

where

$$\mathcal{A} = \frac{2}{3\lambda}\left[\frac{C(\rho_s - \rho) + \rho}{a_T\,\rho_s\,\sin\varphi_{qs}}\right]^{1/2}\frac{\sqrt{g\,h\sin\theta}}{U_0}\,\frac{h}{d_s} \tag{10}$$

and a_T is an empirical coefficient, taking the values 0.04 and 0.35 for rigid and erodible bed, respectively [*Takahashi*, 1978]. A functional relation as (9), however, cannot describe the overall velocity distribution within the mixture, as clearly emerges from the dimensionless plots reported in Figure 11a, where the Bagnold-like profile proposed by *Egashira et al.* [1997], computed by assuming a constant concentration distribution, is also shown.

In order to describe a velocity profile with a downward concavity near the bed and a nearly linear trend in the upper portion of the mixture column, we then consider a power law of the following form:

$$\tilde{u} = k_0\,\tilde{y}^{\beta}. \tag{11}$$

Figure 11b shows the profile described by this equation, obtained by computing the norm of the difference between observed and fitted data, and minimizing it through the Nelder-Mead direct search algorithm, i.e., a multidimensional unconstrained nonlinear minimization method [*Venkataraman*, 2009]. Table 4 summarizes the fitting coefficients k_0 and β obtained by considering the entire set of observed profiles, as done in

Table 4. Coefficients of the Power Law $u = k_0 \tilde{y}^{\beta}$ That Minimizes the Norm of the Differences Between Observed and Fitted Dimensionless Velocity Profiles and the Corresponding Coefficient of Determination, R^2, and Root-Mean-Square Error, RMSE

Material	k_0	β	R^2	RMSE
All data	1.11	1.79	0.93	0.09
Gravel 5 mm	1.01	1.83	0.88	0.11
Gravel 3 mm	1.05	1.67	0.95	0.06
Glass spheres	1.43	2.20	0.97	0.06

Figure 11, or the fitting curves obtained for each type of sediment. The values attained by β are quite similar for 3 mm and 5 mm gravel ($\beta = 1.67$ and 1.83, respectively), while a little bit larger value ($\beta = 2.2$) is found for 3 mm glass spheres. These values, as well as the gradual change in the inclination of profiles, suggest that the mixture rheology does follow neither a viscous regime ($\beta = 2$) nor a dilatant regime ($\beta = 1.5$), as described by Takahashi's dilatant model. This latter regime should however establish in the upper portion of the mixture column, where grain collision stresses tend to prevail. Possible explanations of this deviation from the dilatant behavior can be related to an intermittency of the dominating rheological regime, switching alternately from the collisional to frictional one [*Armanini et al.*, 2009], a coexistence of the two regimes, or a dependence of the ratio $\tau/\sigma_e = f(I)$ on the shear rate at other locations. In this latter case, $f(I)$ is not constant (as implied by a Bagnold-like behavior), but can vary along the flow depth. The possible dependence of the shear stresses at a given point on the shear rates at nearby locations across the flow has been termed as nonlocal rheology by *GDRMiDi* [2004].

In order to address a rheology that can vary along the flow column as a consequence of the overlapping or the intermittency of different generating stress mechanisms, following *GDRMiDi* [2004] and in analogy with Prandtl mixing length framework, we introduce a coherence length $\ell(y)$ such that

$$\tau = \rho_m \ell^2 \dot{\gamma}^2 \tag{12}$$

where τ ($= \rho_m g(h - y)\sin\theta$) is the local value of the mixture shear stress and ρ_m ($= (\rho_s - \rho_f)c + \rho_f$) is the local mixture density. As pointed out by *Tennekes and Lumley* [1972], the mixing length approach strictly would require the existence of univocal velocity and length scales. However, the presence of different stress-generating mechanisms implies the existence of multiple scales. In our case, the velocity scale of the upper layer ($\sim\sqrt{gh\sin\theta}$) is dictated by the destabilizing action of the gravity while the length scale is $\sim d_s$. Less clear is the identification of the relevant scales in the proximity of the static bed, where the contacts among particles are not instantaneous but become long lasting and could involve various particles at the same time. The length scale is possibly related to the size of longitudinal clusters of particles that move along superimposed layers, as suggested by *Jenkins* [2007].

The problem of adopting a mixing length approach involving multiple length scales is common when modeling the atmospheric boundary layer over canopies [*Harman and Finnigan*, 2007]. Usually, the arguments and justification for these scales are empirical and the assessment of their reliability is made through comparison of field measurements with modeled mean velocity, turbulent stress, and longitudinal and vertical velocity variances [*Katul and Chang*, 1999]. Following this heuristic approach, as also proposed by *GDRMiDi* [2004], and recalling equation (12) we estimated the coherence length from the relation

$$\ell(y) = \frac{\sqrt{g(h - y)\sin\theta}}{\dot{\gamma}(y)} \tag{13}$$

where $\dot{\gamma}(y)$ has been determined on the basis of the measured velocity profiles.

Figure 12a shows the values of ℓ obtained from the present experiments. The coherence length, in general, tends to increase as it approaches the static bed. The constant value (of the order of 1–2 d_s) implied by a Bagnold-like profile is attained only in the upper, collision-dominated layer. Near the underlying static sediment bed, long-lasting contacts involve longitudinal clusters of many particles, resulting in much smaller velocity gradient and, hence, larger coherence lengths.

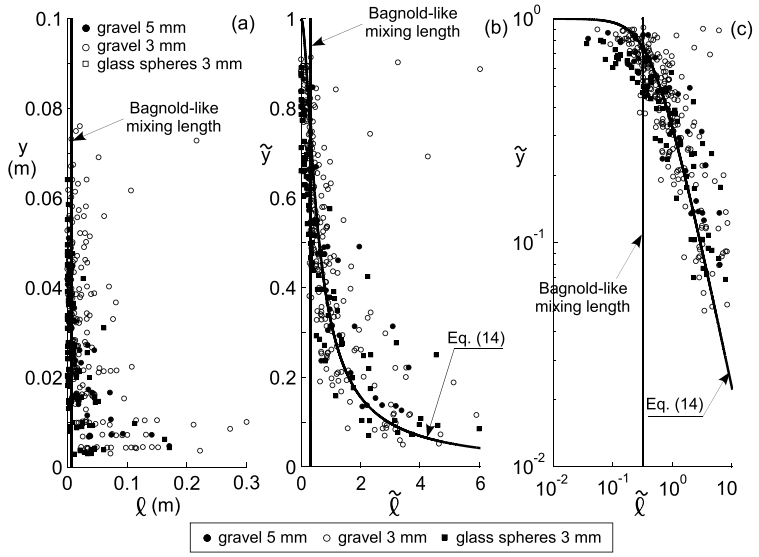

Figure 12. (a) Distribution of coherence length along the direction normal to the flow, computed by means of equation (13) for all the experimental data set provided by *Lanzoni* [1993]. (b, c) Dimensionless plot of the observed coherence length and of the corresponding theoretical distribution provided by equation (14) with $\beta = 1.79$, $k_0 = 1.11$.

The fact that the flow rheology is spatially varying and hence requires multiple length scales reflects on the velocity profile. Computing $\dot{\gamma}$ by means of the functional relationship (11) used to describe analytically the observed profiles, and inserting it into equation (13), we obtain a dimensionless coherence length of the form

$$\tilde{\ell} = \frac{1}{\beta k_0} \tilde{y}^{1-\beta} (1 - \tilde{y})^{1/2} \tag{14}$$

where

$$\tilde{\ell} = \frac{\ell}{h} \frac{U_0}{u_*} \left(\frac{h}{H}\right)^{3/2} \tag{15}$$

Figure 12b shows the comparison between the dimensionless coherence length profile provided by this relation and the observed data. The theoretical coherence length grows significantly when moving toward the static bed, exhibits an inflection point close to $\tilde{y} \sim 0.35$, and tends to zero near to the water surface. This composite behavior is analogous to that encountered in turbulent boundary layers, where the linear mixing length distribution initially postulated by Prandtl has to be suitably modified to account for the deviation of the velocity from the log-law distribution as the wall and the free surface are approached [*Wilcox*, 1993].

5. Conclusions

Taking advantage of a large data set obtained from flume tests in which coarse-grained debris flows were triggered by releasing a given water discharge over a saturated loose sediment bed, we attempted to describe in terms of dominant rheologies the velocity profiles that establish over an erodible bed. The considered data set, obtained under controlled experimental conditions, can also be used to develop and validate numerical codes simulating the inception and subsequent routing of a stony debris flow wave. The conclusions of our analysis can be summarized as follows.

The analysis carried out in the space of the relevant dimensionless parameters (Bagnold, Savage, Reynolds, Friction, Mass, Darcy, and Stokes numbers) suggests that scale effects, associated with the reduced size of the experimental setup and the use of pure water as interstitial fluid appear to be acceptable when the sediment composition of the full size flow has a coarse grain size distribution and the content of fines composing the interstitial slurry is moderate. The values attained by the Stokes and Darcy numbers suggest that excess pore pressure dissipates quite rapidly in the flume tests and, possibly, in a number of debris flows observed at field sites. The role of an increasing content of fines in enhancing nonnegligible excess pore fluid pressure surely merits further investigations, especially in relation to the rate and style of entrainment across the experimental parameter space.

The velocity profiles measured within the body of the flow suggest the presence of regions where different momentum transport processes either dominate or overlap. Frictional stresses tend to prevail in the lower region of the flow, whereas collision stresses dominate or coexist with frictional stresses, in the upper flow layer. These stress-generating mechanisms are apparent in the velocity profiles, which exhibit an upper, almost linear increase, a lower concave down distribution that tends asymptotically to vanish toward the underlying static sediment bed, and a usually smooth transition in between. Because of the coexistence of different physical processes acting at overlapping scales, the velocity profiles are poorly represented by a fixed non-Newtonian rheology. A heuristic approach, based on the coherence length concept, helps to disclose the features of a spatially varying rheology. A Bagnold-like profile, postulating the predominance of collision stresses and implying a constant coherence length, cannot reproduce the observed velocity distributions. The role of quasi-static interactions is in fact crucial for reproducing correctly the velocity profile close to the bottom and the local flow resistance, as confirmed by the coherence length behavior.

Experimental data suggest that the depth-averaged velocity U depends on the triggering discharge, while the flow depth h and the bulk transport concentration C are mainly controlled by the grain size. A remarkable collapse of all the observed velocity profiles is attained independently of the adopted material and of the amount of water used to trigger the flow if the runoff velocity (equation (1)) is chosen as normalization scale. A power law profile, with exponent in the range 1.7 – 2.2 is found to satisfactorily describe the observed velocity distributions.

In the absence of an appreciable excess basal pore fluid pressure, equation (8) describes the functional dependency of the bulk transport concentration on the slope angle and the sediment characteristics, embodied by the quasi-static friction angle φ_{qs} associated with prolonged interparticle contacts. The shape of sediment particles appears to exert a significant role in hampering/enhancing particle sliding, e.g., such that φ_{qs} tends to its static counterpart for spherical grains. Clearly, an important aspect that deserves attention concerns the role that the along-depth distribution of sediment concentration can have in determining the shape of the velocity profile.

Notation

a_T Empirical coefficient.
$\mathcal{A}$ Constant denoting an auxiliary relation.
B Flume width.
c Local concentration.
C Transport (bulk) sediment concentration.
C_{cond} Conductance coefficient.
C_{max} Closest packing sediment concentration.
C_{th} Concentration computed according to equation (8).
D Thickness of the loose sediment bed.
d_s Mean grain size.
g Gravitational constant.
h Debris flow depth with respect to the initial bed elevation.
H Distance from the free surface to the point at which the velocity becomes 1% of that at free surface.
k Hydraulic permeability.
k_0 Coefficient of the power law velocity profile (equation (11)).
ℓ Coherence length.
$\tilde{\ell}$, Dimensionless coherence length.
I Inertial number.
N_{Ba} Bagnold number.
N_{Da} Darcy number.
N_f Friction number.
N_m Mass number.
N_{Re} Reynolds number.
N_{Sa} Savage number.
N_{St} Stoke number.
p_b Basal pore fluid pressure.

p'_b Excess pore fluid pressure.
Q = Total water discharge ($Q_0 + Q_T$).
Q_0 Seepage discharge.
Q_S Volumetric sediment discharge.
Q_{SL} Solid- liquid discharge.
Q_T Triggering water discharge.
t_{ai} Time needed for a particle to move a distance of one grain size through the liquid.
t_{av} Time of deceleration due to Stokes viscous drag force.
t_p Timescale associated to particle rearrangement under the action of confining pressure.
$T_i^{(s)}$ Inertial stresses associated to particle collisions.
$T_q^{(s)}$ Quasi-static stresses associated to long-lasting contacts of sediment grains.
$T_t^{(f)}$ Turbulent fluid stresses.
$T_v^{(f)}$ Viscous fluid stresses.
$T^{(s-f)}$ Interaction stresses due to the relative fluid-grain motion.
u Longitudinal component of the layer-averaged (binned) velocity.
u_f Longitudinal component of the Liquid phase velocity.
u_p Longitudinal component of the particle velocity.
u_s Longitudinal component of the Solid phase velocity.
u_* Friction velocity.
$\hat{u}$ Dimensionless longitudinal velocity u/u_*.
$\tilde{u}$ Dimensionless longitudinal velocity (u/U_0).
U Depth-averaged debris flow velocity.
U_0 Runoff velocity.
U_f Speed of the debris flow front.
U_{tail} Speed of the debris flow tail.
v Normal component of the layer-averaged (binned) velocity.
v_p Normal component of particle velocity.
V_f Liquid volume of the sampled mixture.
V_s Sediment volume of the sampled mixture.
x Longitudinal coordinate.
y Normal coordinate.
$\hat{y}$ Dimensionless normal coordinate (y/H).
$\tilde{y}$ Dimensionless normal coordinate ($(y + H - h)/H$).
α Coefficient depending on the size distribution of particles and the deformation of the mixture.
β Exponent of the power law velocity profile (equation (11)).
$\dot{\gamma}$ Shear rate ($\mathrm{d}u/\mathrm{d}y$).
θ Bed slope angle.
λ Linear concentration.
μ_f Fluid viscosity.
ρ_f Fluid density.
ρ_s Sediment density.
σ_b Total basal normal stress.
σ_e Effective basal normal stress.
τ Shear stress.
τ_0 Basal bed shear stress.
φ_d Dry repose angle.
φ_s Submerged repose angle.
φ_{qs} Quasi-static friction angle.

Acknowledgments
This work was supported by the project "GIS-based integrated platform for Debris Flow Monitoring, Modeling, and Hazard Mitigation", funded by CARIPARO foundation. The authors thank L. Hsu, J. Kean, M. G. Kleinhans, and another anonymous reviewer for the useful comments and suggestions that helped to improve significantly the manuscript. The authors are also indebted to M. Larcher for providing the experimental data on PVC pellets, and A. Armanini for the fruitful discussions. Supporting data are included in the SI file; any additional data may be obtained by contacting the corresponding author.

References

Aragon, G., and A. Juan (1995), Granular-fluid chute flow: Experimental and numerical observations, *J. Hydraul. Eng.*, *121*(4), 355–364, doi:10.1061/(ASCE)0733-9429(1995)121:4(355).
Arattano, M., and L. Franzi (2004), Analysis of different water-sediment flow processes in a mountain torrent, *Nat. Hazards Earth Syst. Sci.*, *4*, 783–791, doi:10.5194/nhess-4-783-2004.
Armanini, A. (2015), Closure relations for mobile bed debris flows in a wide range of slopes and concentrations, *Adv. Water Resour.*, *81*, 75–83, doi:10.1016/j.advwatres.2014.11.003.

Armanini, A., H. Capart, L. Fraccarollo, and M. Larcher (2005), Rheological stratification in experimental free-surface flows of granular-liquid mixtures, *J. Fluid Mech.*, *532*, 269–319, doi:10.1017/S0022112005004283.
Armanini, A., M. Larcher, and L. Fraccarollo (2009), Intermittency of rheological regimes in uniform liquid-granular flows, *Phys. Rev. E*, *79*(5), 051306, doi:10.1103/PhyRevE.79.051306.
Armanini, A., M. Larcher, E. Nucci, and M. Dumbser (2014), Submerged granular channel flows driven by gravity, *Adv. Water Resour.*, *63*, 1–10, doi:10.1016/j.advwatres.2013.10.007.
Badoux, A., C. Graf, J. Rhyner, R. Kuntner, and B. W. McArdell (2008), A debris-flow alarm system for the Alpine Illgraben catchment: Design and performance, *Nat. Hazards*, *49*(3), 517–539, doi:10.1007/s11069-008-9303-x.
Bagnold, R. (1954), Experiments on a gravity-free dispersion of large solid spheres in a Newtonian fluid under shear, *Proc. R. Soc. A*, *225*, 49–63.
Bennett, G., P. Molnar, B. McArdell, and P. Burlando (2014), A probabilistic sediment cascade model of sediment transfer in the Illgraben, *Water Resour. Res.*, *50*, 1225–1244, doi:10.1002/2013WR013806.
Berger, C., B. W. McArdell, and F. Schlunegger (2011), Direct measurement of channel erosion by debris flows, Illgraben, Switzerland, *J. Geophys. Res.*, *116*, F01002, doi:10.1029/2010JF001722.
Berti, M., and A. Simoni (2005), Experimental evidences and numerical modelling of debris flow initiated by channel runoff, *Landslides*, *2*(3), 171–182, doi:10.1007/s10346-005-0062-4.
Berti, M., R. Genevois, A. Simoni, and P. R. Tecca (1999), Field observations of a debris flow event in the Dolomites, *Geomorphology*, *29*, 265–274, doi:10.1016/S0169-555X(99)00018-5.
Berti, M., R. Genevois, R. LaHusen, A. Simoni, and P. R. Tecca (2000), Debris flow monitoring in the Acquabona watershed on the Dolomites (Italian alps), *Phys. Chem. Earth B*, *25*(9), 707–715, doi:10.1016/S0169-555X(99)00018-5.
Berzi, D., J. Jenkins, and M. Larcher (2010), Debris flows: Recent advances in experiments and modeling, *Adv. Geophys.*, *52*, 103–138, doi:10.1016/S0065-2687(10)520002-8.
Cannon, S., J. Gartner, R. C. Wilson, J. C. Bowers, and J. Laber (2008), Storm rainfall conditions for floods and debris flows from recently burned areas in southwestern Colorado and southern California, *Geomorphology*, *96*(3), 250–269, doi:10.1016/j.geomorph.2007.03.019.
Cassar, C., M. Nicolas, and O. Pouliquen (2005), Submarine granular flows down inclined planes, *Phys. Fluids*, *17*(10), 103301, doi:10.1063/1.2069864.
Chou, H. T., Y. L. Chang, and S. C. Zhang (2013), Acoustic signals and geophone response of rainfall-induced debris flows, *J. Chin. Inst. Eng.*, *36*(3), 335–347, doi:10.1080/02533839.2012.730269.
Coe, J., D. Kinner, and J. Godt (2008), Initiation conditions for debris flows generated by runoff at Chalk Cliffs, central Colorado, *Geomorphology*, *96*(3), 270–297, doi:10.1016/j.geomorph.2007.03.017.
Contreras, S., and T. Davies (2000), Coarse-grained debris-flows: Hysteresis and time-dependent rheology, *J. Hydraul. Eng.*, *126*(12), 938–941, doi:10.1061/(ASCE)0733-9429.
Coussot, P., D. Laigle, M. Arattano, A. Deganutti, and L. Marchi (1998), Direct determination of rheological characteristics of debris flow, *J. Hydraul. Eng.*, *124*(8), 865–868, doi:10.1061/(ASCE)0733-9429.
Cui, P., C. Zeng, and Y. Lei (2015), Experimental analysis on the impact force of viscous debris flow, *Earth Surf. Processes Landforms*, *40*, 1644–1655, doi:10.1002/esp.3744.
da Cruz, F., S. Emam, M. Prochnow, J. Roux, and F. Chevoir (2005), Rheophysics of dense granular materials: Discrete simulation of plane shear flows, *Phys. Rev. E*, *72*(2), 021309, doi:10.1103/PhysRevE.72.021309.
de Haas, T., L. Braat, J. R. F. W. Leuven, I. R. Lokhorst, and M. G. Kleinhans (2015), Effects of debris flow composition on runout, depositional mechanisms, and deposit morphology in laboratory experiments, *J. Geophys. Res. Earth Surf.*, *120*, 1949–1972, doi:10.1002/2015JF003525.
Egashira, S., K. Miyamoto, and T. Itoh (1997), Constitutive equations of debris flow and their applicability, paper presented at 1st International Conference on Debris-Flow Hazards Mitigation: Mechanics, Prediction, and Assessment, pp. 340–349, ASCE.
GDRMiDi (2004), On dense granular flows, *Eur. Phys. J. E*, *14*(4), 341–365, doi:10.1140/epje/i2003-10153-0.
Gregoretti, C. (2000), The initiation of debris flow at high slopes: Experimental results, *J. Hydraul. Res.*, *38*(2), 83–88, doi:10.1080/00221680009498343.
Gregoretti, C. (2008), Inception sediment transport relationships at high slopes, *J. Hydraul. Eng.*, *134*(11), 1620–1629, doi:10.1061/(ASCE)0733-9429(2008)134:11(1620).
Gregoretti, C., and G. Dalla Fontana (2008), The triggering of debris flow due to channel-bed failure in some alpine headwater basins of the Dolomites: Analyses of critical runoff, *Hydrol. Processes*, *22*(13), 2248–2263, doi:10.1002/hyp.6821.
Gregoretti, C., M. Degetto, and M. Boreggio (2016a), GIS-based cell model for simulating debris flow runout on a fan, *J. Hydrol.*, *534*, 326–340, doi:10.1016/j.jhydrol.2015.12.054.
Gregoretti, C., M. Degetto, M. Bernard, G. Crucil, A. Pimazzoni, G. Devido, M. Berti, A. Simoni, and S. Lanzoni (2016b), Runoff of small rocky headwater catchments: Field observations and hydrological modeling, *Water Resour. Res.*, *52*, 8138–8158, doi:10.1002/2016WR018675.
Hanes, D., and D. Inman (1985), Observations of rapidly flowing granular-fluid materials, *J. Fluid Mech.*, *150*, 357–380.
Harman, I., and J. Finnigan (2007), A simple unified theory for flow in the canopy and roughness sublayer, *Boundary Layer Meteorol.*, *123*(2), 339–363, doi:10.1007/s10546-006-9145-6.
Hotta, N. (2012), Basal interstitial water pressure in laboratory debris flows over a rigid bed in an open channel, *Nat. Hazards Earth Syst. Sci.*, *12*(8), 2499–2505, doi:10.5194/nhess-12-2499-2012.
Hsu, L., W. E. Dietrich, and L. S. Sklar (2008), Experimental study of bedrock erosion by granular flows, *J. Geophys. Res.*, *113*, F02001, doi:10.1029/2007JF000778.
Iverson, R. (1997), The physics of debris flows, *Rev. Geophys.*, *35*(3), 245–296, doi:10.1029/97RG00426.
Iverson, R., and R. Denlinger (2001), Flow of variably fluidized granular masses across three-dimensional terrain: 1. Coulomb mixture theory, *J. Geophys. Res.*, *106*(B1), 537–552, doi:10.1029/2000JB900329.
Iverson, R., and D. L. George (2014), A depth-averaged debris-flow model that includes the effects of evolving dilatancy, *Proc. R. Soc. A*, *470*, 201330819, doi:10.1098/rspa.2013.0819.
Iverson, R., and J. Vallance (2001), New views of granular mass flows, *Geology*, *29*(2), 115–118, doi:10.1130/0091-7613(2001).
Iverson, R., M. Logan, R. LaHusen, and M. Berti (2010), The perfect debris flow? Aggregated results from 28 large-scale experiments, *J. Geophys. Res.*, *115*, F03005, doi:10.1029/2009JF001514.
Iverson, R. M. (2012), Elementary theory of bed-sediment entrainment by debris flows and avalanches, *J. Geophys. Res.*, *117*, F03006, doi:10.1029/2011JF002189.
Iverson, R. M., and C. Ouyang (2015), Entrainment of bed material by Earth-surface mass flows: Review and reformulation of depth-integrated theory, *Rev. Geophys.*, *53*, 27–58, doi:10.1002/2013RG000447.

Jenkins, J. (2007), Dense inclined flows of inelastic spheres, *Granular Matter*, *10*(1), 47–52, doi:10.1007/s10035-007-0057-z.
Kaitna, R., W. E. Dietrich, and L. Hsu (2014), Surface slopes, velocity profiles and fluid pressure in coarse-grained debris flows saturated with water and mud, *J. Fluid Mech.*, *741*, 377–403, doi:10.1017/jfm.2013.675.
Kaitna, R., M. C. Palucis, B. Yohannes, K. M. Hill, and W. E. Dietrich (2016), Effects of coarse grain size distribution and fine particle content on pore fluid pressure and shear behavior in experimental debris flows, *J. Geophys. Res. Earth Surf.*, *121*, 415–441, doi:10.1002/2015JF003725.
Katul, G., and W. Chang (1999), Principal length scales in second-order closure models for canopy turbulence, *J. Appl. Meteorol.*, *38*(11), 1631–1643, doi:10.1175/1520-0450(1999)038.
Kean, J., S. McCoy, G. Tucker, D. Staley, and J. Coe (2013), Runoff-generated debris flows: Observations and modeling of surge initiation, magnitude, and frequency, *J. Geophys. Res. Earth Surf.*, *118*, 2190–2207, doi:10.1029/jgrf20148.
Kean, J. W., D. M. Staley, R. J. Leeper, K. M. Schmidt, and J. E. Gartner (2012), A low-cost method to measure the timing of postfire flash floods and debris flows relative to rainfall, *Water Resour. Res.*, *48*, W05516, doi:10.1029/2011WR011460.
Koltermann, C. E., and S. M. Gorelick (1995), Fractional packing model for hydraulic conductivity derived from sediment mixtures, *Water Resour. Res.*, *31*(12), 3283–3297, doi:10.1029/95WR02020.
Lanzoni, S. (1993), Meccanica di miscugli solido-liquido in regime granulo-inerziale, PhD thesis, Univ. of Padova (in Italian), Padua, Italy.
Lanzoni, S., and M. Tubino (1993), Rheometric experiments on mature debris flows, paper presented at Congress of International Association for Hydraulic Research (IAHR'93), vol. 3, pp. 47–54, Netherlands.
Larcher, M., L. Fraccarollo, A. Armanini, and H. Capart (2007), Set of measurement data from flume experiments on steady uniform debris flows, *J. Hydraul. Res.*, *45*(1), 59–71, doi:10.1080/00221686.2007.9521833.
Mainali, A., and N. Rajaratnam (1994), Experimental study of debris flows, *J. Hydraul. Eng.*, *120*(1), 104–123, doi:10.1061/(ASCE)0733-9429(1994).
Major, J. (2000), Gravity-driven consolidation of granular slurries: Implications for debris flow deposition and deposit characteristics, *J. Sediment. Res.*, *10*(1), 64–83.
Major, J., and T. Pierson (1992), Debris flow rheology: Experimental analysis of fine-grained slurries, *Water Resour. Res.*, *28*(3), 841–857, doi:10.1029/91WR02834.
Marchi, L., M. Arattano, and A. M. Deganutti (2002), Ten years of debris-flow monitoring in the Moscardo Torrent (Italian Alps), *Geomorphology*, *46*, 1–17, doi:10.1016/S0169-555X(01)00162-3.
McCoy, S., J. Kean, J. Coe, G. Tucker, D. Staley, and T. Wasklewicz (2012), Sediment entrainment by debris flows: In situ measurements from the headwaters of a steep catchment, *J. Geophys. Res.*, *117*, F03016, doi:10.1029/2011JF002278.
McCoy, S., G. Tucker, J. Kean, and J. Coe (2013), Field measurement of basal forces generated by erosive debris flows, *J. Geophys. Res. Earth Surf.*, *118*, 589–602, doi:10.1002/jgrf.20041.
McCoy, S. W., J. W. Kean, J. A. Coe, D. M. Staley, T. A. Wasklewicz, and G. E. Tucker (2010), Evolution of a natural debris flow: In situ measurements of flow dynamics, video imagery, and terrestrial laser scanning, *Geology*, *38*(8), 735–738, doi:10.1130/G30928.1.
Medina, V., M. Hurlimann, and A. Bateman (2008), Application of FLATModel, a 2D a finite volume code to debris flows in the northeastern part of the Iberian Peninsula, *Landslide*, *5*, 127–142, doi:10.1007/s10346-007-0102-3.
Nikora, V., D. Goring, I. McEwan, and G. Griffiths (2001), Spatially averaged open-channel flow over rough bed, *J. Hydraul. Eng.*, *127*(2), 123–133, doi:10.1061/(ASCE)0733-9429(2001)127:2(123).
Okano, K., H. Suwa, and T. Kanno (2012), Characterization of debris flows by rainstorm condition at a torrent on the Mount Yakedake volcano, Japan, *Geomorphology*, *136*, 88–94, doi:10.1016/j.geomorph.2011.04.006.
Parsons, J., K. Whipple, and A. Simoni (2001), Experimental study of the grain-flow, fluid-mud transition in debris flows, *J. Geol.*, *109*(4), 427–447, doi:10.1086/320798.
Rickenmann, D., D. Laigle, B. W. McArdell, and J. Huebl (2006), Comparison of 2D debris-flow simulation models with field events, *Comput. Geosci.*, *10*(2), 241–264, doi:10.1007/s10596-005-9021-3.
Savage, S., and K. Hutter (1989), The motion of a finite mass of granular material down a rough incline, *J. Fluid Mech.*, *199*, 177–215, doi:10.1017/S0022112089000340.
Savage, S., and R. Iverson (2003), Surge dynamics coupled to pore-pressure evolution in debris flows, paper presented at 3rd International Conference on Debris-Flow Hazards Mitigation: Mechanics, Prediction, and Assessment, vol. 1, pp. 503–514.
Stancanelli, L., S. Lanzoni, and E. Foti (2015), Propagation and deposition of stony debris flows at channel confluences, *Water Resour. Res.*, *51*, 5100–5116, doi:10.1002/2015WR017116.
Suwa, H., K. Okano, and T. Kanno (2009), Behavior of debris flows monitored on test slopes of Kamikamihorizawa Creek, Mount Yakedake, Japan, *Int. J. Erosion Control Eng.*, *2*(2), 33–45, doi:10.13101/ijece.2.33.
Suwa, H., K. Okano, and T. Kanno (2011), Forty years of debris flow monitoring at Kamikamihorizawa Creek, Mount Yakedake, Japan, in *5th International Conference on Debris-Flow Hazards Mitigation: Mechanics, Prediction, and Assessment*, vol. 1, edited by R. Genevois, D. L. Hamilton, and A. Prestininzi, pp. 605–613, Casa Editrice Università La Sapienza, Roma, Italy.
Takahashi, T. (1978), Mechanical characteristics of debris flow, *J. Hydraul. Div. ASCE*, *104*(8), 1153–1169.
Takahashi, T. (2007), *Debris Flow: Mechanics, Prediction and Countermeasures, Balkema-Proc. and Monogr. in Eng., Water and Earth Sci.*, Taylor and Francis, New York.
Tennekes, H., and J. Lumley (1972), *A First Course in Turbulence*, MIT Press, Cambridge, Mass.
Thiene, M., W. D. Shaw, and R. Scarpa (2016), Perceived risks of mountain landslides in Italy: Stated choices for subjective risk reductions, *Landslide*, 1–13, doi:10.1007/s10346-016-0741-3.
Tiranti, D., and C. Deangeli (2015), Modeling of debris flow depositional patterns according to the catchment and sediment source area characteristics, *Front Earth Sci.*, *3*, 8, doi:10.3389/feart.2015.00008.
Tognacca, C., G. R. Bezzola, and H. E. Minor (2000), Threshold criterion for debris flow initiation due to channel bed failure, in *Debris-flow hazards Mitigation: Mechanics, Prediction and Assessment*, vol. 30, edited by G. F. Wieczoreck and N. D. Nasser, pp. 89–97, A. A. Balkema, Rotterdam, Netherlands.
Tsubaki, T., H. Hashimoto, and T. Suetsugi (1983), Interparticle stresses and characteristics of debris flows, *Hydrosci. Hydrraul. Eng.*, *1*, 67–82.
Venkataraman, P. (2009), *Applied Optimization with MATLAB Programming*, John Wiley, New York.
Wilcox, D. C. (1993), *Turbulence Modeling for CFD*, DCW Industries, La Cañada, Calif.

Erratum

In section 2.2 of the originally published version of this article, the first sentence misstated that a value was "set equal to 0.001 on the basis of the experiments carried out by Gregotti (2018)." The correct value is 3.0. The error has been corrected, and this may be considered the authoritative version of record.